Key signatures of magnetofossils elucidated by mutant magnetotactic bacteria and micromagnetic calculations

Matthieu Amor, Juan Wan, Ramon Egli, Julie Carlut, Christophe Gatel, Ingrid Marie Andersen, Etienne Snoeck, Arash Komeili

Key signatures of magnetofossils elucidated by mutant magnetotactic bacteria and micromagnetic calculations

Matthieu Amor[1,2*], Juan Wan[1*], Ramon Egli[3,4*], Julie Carlut[4], Christophe Gatel,[5,6] Ingrid Marie Andersen[5], Etienne Snoeck[5], Arash Komeili[1,7]

[1] Department of Plant and Microbial Biology, University of California, Berkeley, CA 94720-3102

[2] Aix-Marseille University, CNRS, CEA, UMR7265 Bioscience and Biotechnology Institute of Aix-Marseille, CEA Cadarache, Saint-Paul-lez-Durance, F-13108, France

[3] Zentralanstalt für Meteorologie und Geodynamik (ZAMG), Hohe Warte 38, A-1190 Vienna, Austria

[4] Université de Paris, Institut de Physique du Globe de Paris, CNRS, 75005 Paris, France

[5] CEMES CNRS, 29 rue Jeanne Marvig, F-31055 Toulouse, France

[6] Université de Toulouse, F-31077 Toulouse, France

[7] Department of Molecular and Cell Biology, University of California, Berkeley, CA 94720-3200

Corresponding author: ramon.egli@zamg.ac.at (RE)

Key points:

- Sediments containing fossilized magnetotactic bacteria bear magnetic signatures apparently associated with different sources of magnetite particles
- Intact and fold-collapsed single-stranded and multi-stranded magnetosome chains can explain all observed signatures of fossilized magnetotactic bacteria
- We provide criteria for the discrimination of distinct populations of ancient magnetotactic bacteria

Abstract

Magnetotactic bacteria (MTB) produce single- or multi-stranded chains of magnetic nanoparticles that contribute to the magnetization of sediments and rocks. Their magnetic fingerprint can be detected in ancient geological samples and serve as a unique biosignature of microbial life. However, some fossilized assemblages bear contradictory signatures pointing to magnetic components that have distinct origin(s). Here, using micromagnetic simulations and mutant MTB producing looped magnetosome chains, we demonstrate that the magnetofossil biosignature is produced by a combination of single- and multi-stranded chains, and that diagenetically-induced chain collapse, if occurring, must preserve the strong uniaxial anisotropy of native chains. This anisotropy is the key factor for distinguishing magnetofossils from other populations of natural magnetite particles, including those with similar individual crystal characteristics. Furthermore, the detailed properties of magnetofossil signatures depends on the proportion of equant and elongated magnetosomes, as well as on the relative abundances of single- and multi-stranded chains. This work has important paleoclimatic, paleontological and phylogenetic implications, as it provides a novel tool to differentiate distinct MTB lineages according to their chain and magnetosome morphologies, which will enable the tracking of the evolution of some of the most ancient biomineralizing organisms in a time-resolved manner. It also enables a more accurate discrimination of different sources of magnetite particles, which is pivotal for gaining better environmental and relative paleointensity reconstructions from sedimentary records.

Plain language summary

Magnetotactic bacteria (MTB) produce chains of magnetic nanoparticles that contribute to the magnetization of sedimentary rocks. Fossilized chains can be detected in ancient geological samples using magnetic measurements. They provide unique evidence for microbial life. However, remains of fossil MTB possess ambiguous magnetic properties that make their detection problematic. Here, we demonstrate, with the help of numerical simulations and a modified MTB producing looped chains, that the magnetic properties of MTB-rich sediments can be explained by a combination of chains made of single and multiple strands, and that chain collapse in the sediment, if occurring, likely preserves key magnetic properties, enabling the identification of fossil MTB. These properties depend also on the proportion of equidimensional and elongated magnetosomes, as well as on the relative abundances of single- and multi-stranded chains. This work has important implications, as it provides a novel tool to differentiate distinct MTB types according to their chain and magnetosome morphologies, enabling the tracking of the evolution of some of the most ancient mineral-producing organisms. It also enables a more accurate discrimination of different sources of magnetite particles, which helps gaining better environmental and relative paleointensity reconstructions from sedimentary records.

1. Introduction

Magnetite (Fe_3O_4) is a ubiquitous iron oxide found in sediments and sedimentary rocks. It is a major carrier of sediments and rock magnetization used for numerous applications in Earth sciences including paleomagnetic, paleoclimate, paleoenvironmental, paleogeographic and paleontological reconstructions (e.g., Evans and Heller, 2003; Tauxe et al., 2010; Egli et al., 2013). In addition to lithogenic magnetite-bearing minerals (e.g., Chang et al., 2016), sediments contain secondary magnetite crystals formed in situ through diagenetic processes (e.g., Oldfield, 2007; Franke et al., 2007), but are also produced by bacteria participating in the sedimentary iron cycle (e.g., Lovely et al., 1987; Fortin and Langley, 2005; Miot et al., 2009).

Magnetotactic bacteria (MTB) are the only known microorganisms that produce intra-cellular nanoparticles of magnetite in organelles called magnetosomes under a genetically controlled pathway (Uebe and Schüler, 2016). They represent some of the most ancient biomineralizing organisms, with a proposed origin of ~3 Ga (Lin et al., 2017). They are markers of oxic-anoxic transition zones in aquatic and sedimentary environments (Flies et al., 2005; Simmons et al., 2004), making them useful paleoenvironmental indicators (Hesse, 1994; Roberts et al., 2011; Usui et al., 2017; Chang et al., 2018; Wagner et al., 2021). Magnetosomes are assembled in chains, and provide the bacteria with a permanent magnetic dipole for navigation purposes (McCausland and Komeili, 2020). When MTB cells die, their magnetite chains can be trapped into sediments and subsequently fossilized (Petersen et al., 1986; Kopp & Kirschvink, 2008). MTB fossils (hereafter referred to as magnetofossils) can be preserved over geological times and contribute to sedimentary paleomagnetic and environmental records (Roberts et al., 2012; Larrasoaña

et al., 2014; Ouyang et al., 2014). Their unambiguous identification and discrimination from abiotic magnetite would thus provide strong constraints on the evolution of life, biomineralization processes, and environmental conditions over geological times.

Arrangement of single domain (SD) magnetite crystals in linear chains combines two robust magnetofossil identification criteria, size and arrangement (Kopp and Kirschvink, 2008), which are key parameters for a unique magnetic signature among all sources of natural magnetic minerals. Other types of secondary magnetite particles tend to have a wide size distribution exceeding the SD stability range (e.g., Gibbs-Eggar et al., 1999; Faivre et al., 2004; Liu et al., 2005). Most importantly, the special conditions required to form isolated, non-branched strings of abiogenic SD particles (e.g., Ruder et al., 2012) are unlikely to occur frequently in natural sediments. Because the magnetic extraction procedure required to prepare sufficiently concentrated samples for statistically significant TEM observations destroys the native arrangement of SD magnetite crystals in the sediment matrix, the in-situ identification of chain structures is only possible through indirect methods based on magnetic measurements of the bulk sediment. Unfortunately, the identification of magnetofossil signatures with magnetic methods is not always unique (e.g., Roberts et al., 2019). An additional complication arises from the fact that the lack of chain structures (e.g., Weiss et al., 2004) does not necessarily exclude a biological origin of SD magnetite particles, since chain collapses that erase the original magnetic fingerprints might occur during early diagenesis.

First-order reversal curve (FORC) diagrams (Egli, 2021), which rely on the measurement of partial hysteresis curves, can be used to discriminate isolated SD magnetite particles and magnetosome chains from other structures, such as SD particle clusters and

larger lithogenic (titano-)magnetite crystals containing magnetic vortices (VO) or multiple magnetic domains (MD) (Roberts et al., 2017; Lascu et al., 2018), through a sharp signature called the central ridge (Egli et al., 2010; Roberts et al., 2012; Heslop et al., 2014a). Principal component analyses (PCA) of FORC diagrams obtained from magnetofossil-rich sediments (Lascu et al., 2015) and selective FORC measurements of secondary $\lesssim$300 nm magnetite particles through selective chemical leaching (Ludwig et al., 2013) contain signatures of VO or strongly interacting SD particle clusters with a large vertical dispersion around the central ridge, which contribute to 35-65% of the total magnetization (Table 1). FORC diagrams containing these features can be explained by mixtures of (*i*) well-dispersed uniaxial, non-interacting SD particles, or linear chains of such particles, contributing to the central ridge (collectively referred to as UNISD in the following), and (*ii*) non-SD or clustered SD particles contributing to the remaining parts of the FORC distribution. The associated magnetic hysteresis parameters $M_{\mathrm{rs}}/M_{\mathrm{s}}$ and $B_{\mathrm{cr}}/B_{\mathrm{c}}$ (Dunlop, 2002) are close to the theoretical limit for non-interacting SD particles and intact magnetosome chains (Table 1). In particular, hysteresis squareness (the ratio $M_{\mathrm{rs}}/M_{\mathrm{s}}$ of remanent and saturation magnetizations) values $\gtrsim$0.44 are unrealistically large for samples containing non-SD or strongly interacting SD particles associable with 35-65% non-central ridge FORC contributions (Ludwig et al., 2013) (Figure 1).

The UNISD signature of magnetofossil-rich sediments is usually characterized by two narrow coercivity distributions (called biogenic soft, BS, and biogenic hard, BH), which are particularly evident in SD-selective magnetic responses such as the central ridge in FORC diagrams and the AF demagnetization of an anhysteretic remanent magnetization (ARM) (Egli, 2004a; Egli et al., 2010; Heslop et al., 2014a). The peculiar narrowness of

these coercivity distributions is determined by the uniaxial magnetic anisotropy of the chain structure, which, together with the shape anisotropy of equidimensional (BS) and elongated (BH) magnetosomes, yields median coercivities of ~30-50 mT and ~65-80 mT, respectively, for these two components.

The mixed FORC properties of magnetofossil endmembers have been explained with a form of chain collapse by which the linear magnetosome arrangement becomes increasingly randomized after MTB death, leading to the formation of fractal-like magnetosome clusters (Harrison and Lascu, 2014; Chang et al., 2019). Isolated magnetosome chains collapse if bent beyond their elastic limit, due to the magnetostatic attraction between the opposed magnetic poles at their extremities (Shcherbakov et al., 1997; Kiani et al., 2015). Bending forces might be produced by mechanical interactions with sediment particles during mixing in the bioturbated layer, and during compaction. Chains might also be stabilized by electrostatic adhesion onto larger sediment particles, such as clay platelets (Galindo-Gonzalez et al., 2009). The lack of direct in situ observation of magnetofossil structures, the mixed character of the magnetic signature of magnetofossil-rich sediments, and the sometimes-poor definition of characteristic coercivity components, leave margins for contrasting interpretations of some geological materials. Most notable examples include the controversial biogenic origin of magnetite nanoparticles in the Martian meteorite ALH84001 (Thomas-Keprta et al., 2000; Golden et al., 2004; Weiss et al., 2004), and the origin of the sudden rise of SD magnetite concentration during the Paleocene-Eocene thermal maximum (Kent et al., 2003; Kopp et al., 2007; Wang et al., 2013; Wagner et al., 2021).

Extracted magnetosomes obtained from MTB cultures after cell lysis tend to form large clumps with an excessively low hysteresis squareness (Kobayashi et al., 2006; Li et al., 2012) (Table 1, Figure 1). This is also true for the hysteresis squareness of smaller magnetosome clusters produced by MTB whose genes responsible for chain assembly have been deleted, namely the Δ*mamJ* MSR-1 strain in Katzmann et al. (2013) (see sections below), which might serve as analogue for the full collapse of isolated chains. Finally, the random-walk-based magnetosome assemblage algorithm of Harrison and Lascu (2014) produce a range of magnetic properties (Chang et al., 2019) comprised between the endmembers corresponding to linear chains and fractal-like particle clusters, respectively, depending on the assumed degree of randomness (Figure 1). In these simulations, FORC diagrams containing non-UNISD contributions comparable with those of magnetofossil endmembers are associated with hysteresis squareness values of ~0.4 or lower. Pedogenic magnetite, the only well-characterized natural example of non-biogenic secondary magnetite particles (Dearing et al., 2001), also features mixed UNISD and non-UNISD FORC properties (Table 1); however, in this case, the hysteresis squareness of ~0.2 is compatible with the FORC signature. Thus, current interpretations of magnetofossil signatures appear to miss structures possessing the correct combination of UNISD and non-UNISD magnetic properties.

Excluding disordered clusters, which do not possess the correct magnetic signature, and the already investigated chain axis randomization, possible candidates for missing magnetofossil morphologies include native multistranded chains of magnetosomes produced by some MTB (Amor et al., 2020) and mechanically meaningful minimum-energy structures obtained from the collapse of isolated chains, such as rings and double

177 strands resulting from the fold-collapse of single-stranded chains that have been bent
178 beyond the elastic limit (von Dobeneck et al., 1987; Philipse and Maas 2002; Kiani et al.,
179 2018). Single- and multi-stranded chains in MTB and in the derived intact magnetofossils
180 (Figure 2a,b) are in a native SD state that maximizes the total magnetic moment, with the
181 magnetization of all magnetosomes being parallel to the chain axis (Hanzlik et al., 2002).
182 This is the only possible zero-field magnetic configuration for single-stranded chains, but
183 not for multiple strands, in which intermediate states with lower magnetic moments can
184 be nucleated with the application of strong external fields (Hanzlik et al., 2002).
185 Intermediate remanent states are formed when the magnetic moment of one strand is
186 reversed with respect to the others, or when the magnetic moments of individual crystals
187 form complex patterns (Varón et al., 2013). On the other hand, structures arising from
188 chain collapse (Figure 2c,d), are expected to possess native flux-closure (FC)
189 configurations characterized by a small net magnetic moment, as observed for instance in
190 nanoparticle rings (Dunin-Borkowski et al., 2004; Takeno et al., 2014). These
191 configurations minimize the magnetostatic energy by suppressing the external stray field
192 of SD-like magnetic states. The low magnetic moment of collapsed structures makes
193 them a poor sedimentary recorder of the Earth magnetic field, contrary to intact
194 magnetosome chains, so that the fate of fossil magnetosome chains during diagenesis is
195 expected to have important implications for the paleomagnetism of magnetofossil-rich
196 sediments.

197 FORC measurements are sensitive to transitions between high-moment (SD-like) and
198 low-moment (FC-like) magnetic configurations and their in-field stability ranges (Egli,
199 2021). In particular, hysteresis squareness values close to 0.5, typical of randomly

200 oriented UNISD particles, depend on the room-temperature zero-field stability of high-
201 moment states. This stability, which enables MTB to navigate along the Earth magnetic
202 field, has been demonstrated experimentally for native single- and multistranded chains
203 (Hanzlik et al., 2002; Pan et al., 2005), but no information is available for collapsed
204 structures.

205 Here, we demonstrate that the unresolved magnetic signature of magnetofossils (i.e.,
206 FORC signatures typical of magnetostatic interactions and FC, which do not lower the
207 hysteresis squareness typical of UNISD particles) can be explained by the predominant
208 contribution of intact or elastically deformed single- or multi-stranded magnetosome
209 chains (non-collapsed). Contributions from fold-collapsed chains are also possible. Nu-
210 cleation and annihilation of FC magnetic states explains non-UNISD signatures in FORC
211 diagrams of magnetofossil-bearing sediments, while the strong uniaxial anisotropy of
212 intact and fold-collapsed chains ensures that they still possess a UNISD-like hysteresis
213 squareness of ~0.5. Our claim is supported by micromagnetic simulations of native
214 single- and double-stranded chains and fold-collapsed chains. Unfortunately, MTB
215 producing multi-stranded chains are not available for culture in the laboratory; however,
216 the validity of our micromagnetic calculations has been tested by comparing the magnetic
217 signature of intact chains with some structures that may be produced by the spontaneous
218 collapse of isolated chains. For this purpose, we produced a mutant of the magnetotactic
219 bacterium *Magnetospirillum magneticum* strain AMB-1 synthesizing looped structures
220 similar to the rings described by Kiani et al. (2018) and to some structures obtained after
221 dissolution of cultured cells of the same strain (Philipse and Maas, 2002). Looped chains
222 might form in sediment after cell disruption, but before stabilizing structures such as

magnetosome membranes and the connecting cytoskeletal filament (Komeili et al., 2006) are dissolved, owing to the larger elastic response of membrane-filled gaps (Shcherbakov et al., 1997). Fold-collapsed chains, on the other hand, might form after dissolution of all biological structures, as a consequence of the much lower elastic limit associated with contacting magnetosomes (Shcherbakov et al., 1997).

From magnetic measurements and off-axis electron holography characterizations, we show that the looped chains produced by the AMB-1 mutant generate FC magnetic signatures similar to those obtained with our micromagnetic simulations of single- and multi-stranded chains, while lacking the hysteresis squareness of the simulations and of natural magnetofossil signatures. This demonstrates that the unique magnetic fingerprints of magnetofossils originate from strongly uniaxial magnetosome arrangements, rather than clusters, rings, and other forms of looped chains lacking a uniaxial shape. This work resolves longstanding and ongoing controversies about the interpretation of sedimentary sources of SD magnetite, establishing a theoretical and experimental framework that explains the magnetofossil signature and provides insights into the diversity of ancient MTB populations. A glossary of specialized terms used to describe magnetic measurements and micromagnetic modeling results is provided in the Supporting Information.

2. Material and methods

2.1. Micromagnetic modeling

To determine whether native multi-stranded and fold-collapsed magnetosome chains could explain the observed magnetofossil signatures, we modeled their FORC properties.

Micromagnetic models of high-resolution FORC measurements have been calculated for selected magnetosome morphologies and chain configurations representative of intact or elastically deformed chains, and of fold-collapsed chains. The magnetic properties of the simulated structures are determined mainly by two factors: the anisotropy of individual magnetosomes, which is controlled by their shape and crystal orientation, and in-chain magnetostatic interactions, which are controlled mainly by the chain geometry (Berndt et al., 2020). Magnetosome shapes can be classified as equant (cuboctahedral, octahedral), elongated (prismatic, elongated octahedral), and highly elongated (tooth- and bullet-shaped) (Amor et al., 2020). These categories form well-defined clusters of crystal sizes and shapes within the SD stability range of magnetite (Muxworthy and Williams, 2006; Newell, 2009) (Figure S1).

The geometry of intact single-stranded chains is controlled by the gaps between magnetosomes, the size decrease of immature crystals towards the chain extremities (tapering), and chain bending within the elastic limit. Magnetosomes in native multi-stranded chains are staggered: each magnetosome in one strand faces the gap between two magnetosomes of a nearby strand (Figure 2a,b). This arrangement favors the formation of strand bundles with a consistent magnetic polarity, eliminating repulsive forces (Hanzlik et al., 2002; Ruder et al., 2012). Contrastingly, magnetosomes in fold-collapsed chains are arranged side-to-side, and size tapering occurs only at one end, the other end being the kink point of the native chain (Figure 2d). The side-to-side magnetosome arrangement maximizes lateral attractive forces between strands with opposite magnetic polarities (Varón et al., 2013), as they result from fold-collapse. Fold-

collapsed chains can be observed inside freeze-dried cells (e.g., Figure 2b in Lins and Farina, 2004), where collapse is likely induced by cell shrinking.

The full variability of natural chain structures can be only partially reproduced because geometric parameters must be extrapolated from few observations. Therefore, we selected combinations of two magnetosome morphologies (cuboctahedral and prismatic), and three chain geometries (single-stranded, native double-stranded, and double-stranded from collapse by folding), as representative examples of magnetic endmembers dictated by the magnetosome aspect ratio (equant vs. elongated), and the existence of flux-closure configurations (single- vs. double-stranded). We generated ~10^5 synthetic chains with random orientations and realistic geometries for each of the six categories obtained by combining the above-mentioned magnetosome morphologies and chain configurations (see Supporting Information for details).

Micromagnetic modeling has been performed in two steps using an energy minimization method. First, randomly oriented synthetic chains have been generated for each of the six configurations. Magnetosome-specific control parameters include size, shape, and crystal axes orientation, based on realistic distributions obtained from the literature (Figure S1). Chain-specific control parameters include magnetosome gaps, number of crystals, size tapering towards the extremities, and chain bending within the elastic limit. The geometry of double-stranded chains is additionally controlled by the lag of one strand with respect to the other, and by twisting of the two strands about a common axis (Figure 2a). The distributions of these parameters (Table S1) have been empirically chosen to match images reported in the literature. Representative examples of synthetic double-stranded chains are shown in Figures S2-S5. Next, FORC measurements

between ±0.3 T have been simulated in 1 mT steps using a micromagnetic model of the chain magnetization. These calculations are based on the local minimization of the total energy determined by the magnetocrystalline and shape anisotropy of individual crystals, the Zeeman energy in the applied field, and the energy of magnetostatic interactions between pairs of crystals (see the Supporting Information for details). Because FORC measurements consists of a series of field sweeps starting at positive saturation, where there is only one local energy minimum (LEM), the evolution of LEM states is uniquely determined.

Like in Harrison and Lascu (2014), we assumed that individual crystals are homogeneously magnetized, but we calculated magnetostatic interactions for the actual magnetosome shape, instead of using a point dipole approximation. The homogeneous magnetization approximation, which is needed to speed up calculations and cover the whole parameter space with a sufficiently large number of high-resolution FORC simulations, holds reasonably well in all applied fields, including those immediately preceding transitions between magnetic states, for magnetosome sizes up to ~50 nm, as seen by comparison with full micromagnetic models (Berndt et al., 2020). At larger sizes, the validity of this approximation declines progressively, as helical configurations start to nucleate inside the end magnetosomes. Nevertheless, the coercivities of remanence calculated by Berndt et al. (2020) for single-stranded chains of equidimensional and elongated magnetosomes are compatible with the coercivity distributions obtained from our simulations, so that the uncertainty introduced by our approximation is not expected to exceed the uncertainties associated with a poor knowledge of the real distribution of model parameters. Simulated FORC measurements (Figure S6) have been further processed with VARIFORC (Egli,

313 2013), using minimal smoothing parameters ($s = 1$ over the central ridge, and $s = 4$,
314 $\lambda = 0.08$ over the remaining parts of the FORC diagram) to eliminate statistical noise.

315 The role of chain geometry for the stabilization of the remanent magnetization of high-
316 moment states, which is essential for obtaining elevated hysteresis squareness values, has
317 been investigated by calculating the energy barrier that must be overcome for a thermally
318 activated transition to a different state at room temperature. For this purpose, we
319 considered four prototypical arrangements of identical, equidimensional magnetosomes
320 with no intrinsic anisotropy: (1) single-stranded chains, (2) native double-stranded chains,
321 (3) fold-collapsed chains, and (4) circular rings. Optimal transition paths between LEM
322 states have been calculated with the nudge-elastic-band and action minimization
323 technique of Fabian and Shcherbakov (2018), upon identifying the magnetic moments of
324 individual magnetosomes with the magnetic moments of elemental cells used in full
325 micromagnetic simula-tions (see the Supporting Information for details).

326 The choice of an adequate initial path is crucial for obtaining a globally optimized
327 transition between states. Single-stranded chains of >4 crystals are known to reverse their
328 remanent magnetization by nucleation of a reversed domain at one end (Hendriksen et al.,
329 1994; Newell, 2009) and subsequent propagation of this domain to the other end. In this
330 case, an adequate initial approximation of the reversing path is generated from an initial
331 two-domain structure obtained by forcing the magnetic moment of the middle magneto-
332 some to a direction perpendicular to the chain axis. This configuration is then relaxed
333 while the strength of dipolar interactions in one of the two domains is slightly weakened
334 to favor its denucleation (Figure S7a). The high-moment configuration of large rings
335 consists of two domains separated by perpendicular magnetic moments pointing to the

same direction (Figure S7b). The transition to a zero-moment FC state with clockwise or counterclockwise magnetic moment arrangement is simulated in the same manner as for linear chains by denucleating one of the two domains. Finally, the transition path of double-stranded chains from the high-moment state, where the two strands are magnetized in the same direction, to the low-moment state, where the two strands have opposed magnetizations, requires the nucleation of a reversed domain at the extremity of one strand (Figure S7c). The nucleated domain creates an energetically favored FC configuration with the other strand, so that the transition to a complete FC state is obtained by growing the reverse domain until it reaches the other chain extremity.

2.2. Deletion plasmid construction and generation of the Δ*mamJ*Δ*limJ*ΔMIS AMB-1 mutant strain

To obtain a term of comparison for possible collapsed chain configurations and validation of our micromagnetic modeling, we generated a mutant AMB-1 strain with looped magnetosome chains (Figure 3). Magnetosome formation in MTB requires genes contained in a specific portion of the genome called the magnetosome island (MAI) (Murat et al., 2010). The AMB-1 genome also contains a small version of the magnetosome island called the magnetotaxis islet (MIS) (Rioux et al., 2010). The MIS contains several genes, some of which perform redundant functions with their homologs in the MAI (Abreu et al., 2014). Previous work in *Magnetospirillum gryphiswaldense* strain MSR-1, a close relative of AMB-1, showed that the loss of the MAI gene *mamJ* results in collapse and aggregation of magnetosome chains (Scheffel et al., 2006). Surprisingly, the deletion of *mamJ* and its other MAI homolog *limJ* in AMB-1 does not produce collapsed chains and instead results in minor disruptions to the continuity of the

359 chain (Draper et al., 2011). We reasoned that redundant functions within the MIS might
360 account for the dramatic differences between *mamJ* mutants in AMB-1 and MSR-1.
361 Thus, a mutant strain (Δ*mamJ*Δ*limJ*ΔMIS) was produced by deleting the entire MIS and
362 two MAI genes (*mamJ* and *limJ*) from AMB-1 genome. Detailed procedures for plasmid
363 construction and AMB-1 transformation are provided in the Supporting Information.

364 **2.3. Bacterial cultures**

365 *Magnetospirillum magneticum* strain AMB-1 (ATCC700264) and the mutant AMB-1
366 strain described in Section 2.2 were cultivated following ATCC recommendations in 500-
367 mL screw-caped bottles until end of the exponential phase. Bottles were filled with 300
368 mL of growth medium and placed in a glove box with controlled atmosphere (10% O_2,
369 90% N_2) at 30°C after inoculation (1/100). The sole iron source in bacterial growth
370 medium was Fe(III)-citrate added at 150 μM.

371 **2.4. Transmission electron microscopy**

372 Wild type and mutant AMB-1 cells were deposited on copper grids coated with a
373 Formvar and carbon films and characterized with a FEI Tecnai 12 transmission electron
374 microscope operating at 120 kV.

375 **2.5. Native magnetic moment measurements**

376 Magnetic characterizations of the mutant AMB-1 strain suggest that its looped
377 magnetosome chain configurations possess a low net magnetic moment (see section 3.3).
378 We thus investigated the native magnetic state of wild-type and mutant AMB-1 strains at
379 the population level by comparing the magnetization of two different preparations of
380 aqueous cell suspensions in a maximum external field of 2 mT, using a vibrating-sample

magnetometer (VSM). The external field is sufficiently large to partially align the cells, but not large enough to alter their native magnetic configuration. In this case, the magnetization of the suspension is expected to be proportional to the mean strength of the magnetic moments of individual cells. The first preparation contains cells directly taken from the culture and is used to assess the native magnetic moments. In the second preparation, the suspension is previously exposed to a 200 mT field. This field is strong enough to reset the native magnetic states, replacing them with a saturation remanent state that corresponds to the maximum magnetic moment that can be maintained in a null field. Cell suspensions for these experiments were prepared by centrifugation of AMB-1 cultures (8000 rpm, 10 min), and subsequent suspension in 10 mL of phosphate buffer (PBS). 100 μL of cell suspension were transferred in plastic vials (diameter of 4 mm) and placed in a Lakeshore Micro-Mag 3900 VSM for acquisition of remanent magnetizations at room temperature.

2.6. Off-axis electron holography

VSM characterizations of mutant AMB-1 demonstrated a vanishingly small native magnetic moment of the bacteria, which can be explained by the looped chain structures being in a FC state. To further confirm this hypothesis, we mapped the magnetic flux in the looped chains at the single-crystal level with off-axis electron holography. Electron holography is an interferometric method that correlates morphological and local magnetic characterizations of magnetic materials. It allows quantitative mapping of the in-plane flux inside the magnetite chains produced by AMB-1 at the nanometer scale. Both wild-type and mutant AMB-1 strains were cultivated in 10-mL glass tubes following the protocol described above. Cells were centrifuged (8000 rpm, 10 min) and suspended in

100 μL of phosphate buffer (PBS). They were then deposited on copper grids coated with an ultra-thin carbon membrane. Off-axis electron holography was carried out using a Hitachi HF3300C microscope operated at 300 kV and equipped with a cold field emission gun and a spherical aberration corrector (CEOS B-Corr). Electron holography experiments were performed in a specific corrected Lorentz mode, allowing a spatial resolution down to 0.5 nm in a magnetic field-free sample environment (Snoeck et al., 2014). All holograms were recorded in a 2-biprism configuration to avoid artifacts linked to Fresnel fringes and to set separately the interference area size and the fringe spacing (Harada et al., 2004). The fringe spacing is equal to 1 nm (7 pixels) allowing for a spatial resolution of 1.5 nm for the treated magnetic phase images. The exposure time was set to 1 nm using dynamic automation acquisition for removing instabilities and applying the fringe π-shift method (Gatel et al., 2018; Volkov et al., 2013). Phase and amplitude images were extracted from the holograms by using homemade software based on fast-Fourier transform approach. The magnetic and electrostatic contributions have been separated by acquiring two holograms for which the sample has been switched upside down (flipped 180°): the magnetic contribution was obtained by evaluating the difference of the phase images from the two holograms divided by two.

2.7. FORC measurements

The magnetic properties of the wild-type and mutant AMB-1 strains were characterized with high-resolution FORC analyses using a VSM. AMB-1 cultures were recovered by centrifugation (8 000 rpm, 10 min). Bacterial pellets were transferred in a 1.5-mL Eppendorf tube and dried at room temperature under anoxic conditions in a glove box ($[O_2]$ < 1ppm) to prevent magnetite oxidation. Samples were stored under anoxic conditions until

being measured with a Lakeshore 8600 VSM. High-resolution FORC measurements were performed in steps of 0.3 mT with a stepwise approach to the reversal field to avoid over-shooting artifacts (Wagner et al., 2021), and a pause of 1 s at reversal. Measurements have been processed with VARIFORC (Egli, 2013) using a minimum smoothing factor $s = 2$ across the central ridge, and $s = 4$, $\lambda = 0.14$ over the remaining parts of the FORC diagram.

3. Results

3.1 Chain geometry and magnetic states

The existence of one or more than one pair of magnetic states, and the stability of these states against thermal relaxation and applied fields, depends on the interplay between the magnetic anisotropy of individual crystals and the magnetostatic interactions between them. The stabilizing or destabilizing effect of magnetostatic interactions depends in turn on the chain geometry. Because magnetosome elongation is the main factor controlling the magnetic anisotropy of individual crystals, and because elongation, if present, is parallel to the chain axis and has a stabilizing effect, the minimum stability granted by the chain geometry is best investigated assuming equidimensional magnetosomes with no magnetocrystalline anisotropy and purely dipolar interactions, as in Hendriksen et al. (1994). In this case, single-stranded chains possess only one pair of remanent states with all magnetic moments parallel or antiparallel to the chain axis (Figure 4a). For chains with >4 magnetosomes, thermally activated transitions between these two states occur by nucleating a domain with reversed magnetization at one end of the chain (Figure 4b). The two domains with opposed axial moments are separated by a transition region of ~3 crystals with magnetic moments that deviate from the chain axis.

Once the two domains are formed, the transition is completed by moving the transition region towards the other end of the chain, until the original domain is denucleated (Movie S1). The energy barrier that needs to be overcome for this transition is $\Delta E = \beta_0 k_B T$, where k_B is the Boltzmann constant, T the absolute temperature, and β_0 the so-called Boltzmann factor. At room temperature (T = 293 K), $\beta_0 \approx 836$ for N =15 magnetite magnetosomes with a diameter of 50 nm separated by 5 nm gaps. The energy barrier depends only weakly on the number of magnetosomes if $N > 6$ (Table 2). For comparison, the stability threshold predicted by the Néel-Arrhenius law $\tau = \tau_0 \exp(\beta_0)$, where τ is the time constant of the spontaneous magnetization decay and $\tau_0 \approx$ 0.1-1 ns (Moskowitz et al., 1997), is $\beta_0 \approx 59$ for geologic time scales (τ = 1 Ga), ~32 for the typical lifespan of a cell ($\tau \approx$ 1 day), and ~25 for the typical time required to measure a single FORC ($\tau \approx$ 1 min). This yields a lower stability threshold of ~17 nm for $\tau \approx$ 1 min. For comparison, Newell (2009) obtained a threshold of ~15 nm for the same chain geometry and N = 6, using a purely analytical approach and upon including the magneto-crystalline anisotropy of magnetosomes with ⟨111⟩ axes parallel to the chain axis. The latter adds stability to the magnetic moments, explaining the slightly smaller threshold.

The large energy barrier generated by axial magnetostatic interactions ensures that field-induced transitions between the two stable states of single-stranded chains occur in proximity of the theoretical switching fields predicted by micromagnetic models that neglect thermal activations, such as the one used here and those of Harrison and Lascu (2014) and Berndt et al. (2020). Nevertheless, thermal activations are still sufficiently large to produce a measurable vertical offset of the central ridge (Egli, 2013, 2021), due to the intrinsic time asymmetry of the FORC measurement protocol (Berndt et al., 2018).

473 The central ridge offset of high-resolution FORC measurements of magnetofossil-rich
474 sediments, which is of the order of 0.3-0.5 mT (Egli et al., 2010; Ludwig et al., 2013;
475 Wagner et al., 2021), can be explained by a Stoner-Wohlfarth model of thermally
476 activated UNISD particles (Lanci and Kent 2018; Berndt et al., 2018) with $\beta_0 \approx$ 400-600.

477 The high-moment remanent state of magnetosome rings, obtained by decreasing the
478 applied field from saturation to zero, is similar to the "onion state" of toroidal magnetite
479 nanoparticles described by Lewis et al. (2020), in which the magnetic flux enters the ring
480 from one side, flows past the central hole, and exits on the other side (Figure 4c). In the
481 limit case of large rings, the "onion state" is equivalent to two magnetic domains with
482 clockwise and counterclockwise fluxes tangential to the circumference, separated by two
483 transition zones similar to that of a single-stranded chain with two domains (Figure 4b).
484 Deviations from the tangential magnetization in the transition zones point to the in-plane
485 component of the field used to impart a saturation remanence. Unlike the case of single-
486 stranded chains, where most of the energy barrier is associated with the nucleation of a
487 new domain, transitions to a zero-moment FC state (Figure 4d) occur with little
488 additional energy by moving one of the two domain boundaries until it merges with the
489 other boundary, leaving a single domain with circular magnetization (Movie S2). The
490 energy barrier of this transition is $\beta_0 \approx 27$ for a ring made of 20 magnetosomes with 5 nm
491 gaps. The FC state is much more stable, as seen from the energy required for the opposed
492 transition ($\beta_0 \approx 1632$). In practice, the saturation remanence of $N = 20$ rings will decay
493 exponentially to zero (which is the net magnetization of the FC states) in ~9 minutes. The
494 saturation remanence of smaller rings is better stabilized (e.g., $\beta_0 \approx 55$ for $N = 16$), but
495 still much less than single-stranded chains with the same number of magnetosomes.

The high-moment remanent state of double-stranded chains is similar to that of single stranded chains, with the two strands possessing nearly axial moments with same polarity (Thomas et al., 2008) (Figure 4e). The magnetic moments of the end magnetosomes are not completely aligned with the chain axis, due to the reduced axial magnetostatic coupling and the stray field concentration at the chain extremities. Transitions to the low-moment remanent state, where the two strands with opposed polarities form a closed flux loop (Figure 4f), occur by nucleating a reverse domain in one of the two strands. An example can be seen in Figure 10 of Simpson et al. (2005), where two antiparallel domains in one strand are stabilized by a kink. The transition is then accomplished by extending the reverse domain until the original domain is fully denucleated (Movies S3-4). Native double-stranded chains with staggered magnetosomes (Figure 2a,b), and double-stranded chains with facing magnetosomes resulting from fold-collapse (Figure 2d), undergo the same type of transitions between high- and low-moment states; however, the high-moment state of the native double-stranded chains is more stable than that of fold-collapsed chains (e.g., $\beta_0 \approx 751$ vs. 242 for $N = 2\times11$, Table 2), due to the staggered magnetosome arrangement (Hanzlik et al., 2002; Ruder et al., 2012). In both cases, high-moment states are stable over geologic times. The energy barriers that need to be overcome for the reversed transitions, from low- to high-moment states, are slightly larger than those of single-stranded chains.

3.2 Micromagnetic FORC models

Simulated FORC diagrams of single-stranded chains (Figure 5a,d) possess all the expected characteristics UNISD particles (Newell, 2005), also seen in cultured MTB (Li et al., 2012; Jovane et al., 2012; Wang et al., 2013, 2015). These characteristics include

519 (1) a sharp central ridge along $B_u \approx 0$, which is produced by the collective switching of all
520 magnetic moments within individual chains, (2) lack of contributions over the upper qua-
521 drant, and (3) a distribution of positive and negative amplitudes in the lower quadrant,
522 nearly antisymmetric with respect to the $B_c = -B_c$ diagonal, produced by the reversible
523 rotation of the magnetic moments in the applied field (Egli, 2021). FORC measurements
524 define three coercivity distributions (Egli, 2021) associated with (1) irreversible magneti-
525 zation changes along the lower branch of the hysteresis loop (f_{hys}), (2) the remanent
526 magnetization of a so-called DC or backfield demagnetization curve (f_{dcd}), and (3) the
527 central ridge (f_{cr}). In our simulations of single-stranded chains, all three distributions have
528 identical, Gaussian-like shapes dictated by the in-field (f_{irr}, f_{cr}) and zero-field (f_{dcd})
529 magnetic moment changes associated with transitions from negative to positive high-
530 moment states. The coercivity distributions are slightly narrower and biased towards
531 ~30% higher fields with respect to the biogenic components BS and BH commonly found
532 in magnetofossil-rich sediments (Chen et al., 2014; Egli, 2004a; Heslop et al., 2014a).
533 This difference can be explained in part by the fact that micromagnetic calculations were
534 based on stoichiometric magnetite, while real magnetofossils are often partially or
535 completely maghemitized (Vali et al., 1987; Housen and Moskowitz, 2006). The
536 maghemite endmember (γ-Fe_2O_3) has a ~20% lower spontaneous magnetization, and a
537 similar reduction in coercivity is therefore expected. Furthermore, the magnetosome gap
538 in real magnetofossils might be larger than assumed in our calculations, producing a
539 further reduction of the switching field (Berndt et al., 2020).

540 Simulated FORC diagrams of double-stranded chain configurations feature typical
541 flux-closure signatures (Figure 5b,c,e,f) as described in Egli (2021). These features are

542 fully developed only in fold-collapsed chains of equidimensional magnetosomes,
543 resulting in a constricted hysteresis loop (Figure S6e) and clearly identifiable pairs of
544 positive and negative lobes surrounding the central ridge (Figure 5c). These lobes are
545 generated by transitions between high- and low-moment states with different in-field
546 stability ranges (see Egli, 2021, and Figure 57 therein for a detailed explanation). The
547 central ridge, on the other hand, is associated exclusively with the denucleation of FC
548 configurations. Magneto-some elongation and staggering in native double-stranded
549 chains add stability to the high-moment state, as seen by the partial suppression of the
550 negative lobes around the central ridge (Figure 5b,e,f). The only natural example of
551 FORC signature produced by multi-stranded chains is that of a concentrate of wild-type
552 *M. bavaricum* cells extracted from a pond sediment (Roberts et al., 2012). This sample
553 features positive contributions in the upper quadrant of the FORC diagram which might
554 be attributed to the denucleation of FC states.

555 Contrary to the AMB-1 mutant (see below) and other examples of magnetic systems
556 featuring this type of FORC signature, such as single-vortex (SV) particles (Dumas et al.,
557 2007; Katzmann et al., 2013; Roberts et al., 2017), the hysteresis squareness of our mo-
558 delled double-stranded chains is only slightly lowered with respect to the uniaxial SD
559 case (M_{rs}/M_s = 0.471, Table 1, Figure 1), and fully compatible with magnetofossil
560 signatures (Ludwig et al., 2013). Squareness values close to 0.5 for all simulated double-
561 stranded and fold-collapsed chains means that they possess stable SD states in zero field,
562 as observed on native chains (Li et al., 2015), and unlike the looped chains of the AMB-1
563 mutant. Stable high-moment states in zero field require the hysteresis loop to be fully

564 reversible until the applied field reverses sign, which means that the FORC function is
565 fully comprised within the so-called memory region (dashed lines in Figure 5).

566 The central ridge coercivity distributions of double-stranded chains are almost
567 identical to those of single-stranded chains made of the same type of magnetosomes. This
568 is expected from the similar stability of high-moment states in single-stranded chains and
569 of FC states in double-stranded chains (Table 2). Non-central ridge coercivity
570 distributions, on the other hand, contain additional low-field contributions related to the
571 nucleation of FC states. In the case of equant magnetosomes, these contributions produce
572 a second peak (fold-collapsed chains) or a shoulder (native chains) at $B_c \approx 15$ mT. In the
573 case of prismatic magnetosomes, coercivity distributions remain unimodal but become
574 wider, and the peak position is lowered by ~10 mT with respect to the central ridge. Non-
575 central ridge coercivity distributions of native double-stranded chains are remarkably
576 similar to the biogenic coercivity components BS and BH (Figure 5b,e).

577 **3.3 Mutant AMB-1 strain with looped chains**

578 Unlike the Δ*mamJ* MSR-1 mutant, which produces agglomerated clusters of magneto-
579 somes, the phenotype of our AMB-1 mutant contains looped magnetosome chains with
580 necklace structures located either at one of the poles or at the center of the cell (Figure 3).
581 Magnetosomes in the mutant strain fall mostly within the stable SD size range of single-
582 stranded chains (Muxworthy and Williams, 2006; Newell, 2009). The magnetic behavior
583 of bacteria was assessed using the magnetic coefficient (C_{mag}), which relies on the
584 differential measurement of a culture's optical density when a magnet is oriented either
585 vertically or horizontally close to the cell suspension. C_{mag} is defined as the ratio of the
586 maximum and minimum optical density measured and quantifies the capacity of bacteria

587 to orientate along an external magnetic field (Schüler et al., 1995). C_{mag} values at the end
588 of bacterial growth were 1.82 ± 0.09 and 1.09 ± 0.01 for wild-type and mutant AMB-1
589 (three replicates for each strain), respectively, demonstrating a very limited orientation
590 capability for the mutant strain.

591 **3.4 Native magnetic states of wild-type and mutant AMB-1 cells**

592 MTB cells containing ideal magnetite chains possess already a saturation moment.
593 Exposing them to large fields will thus not change the magnetization of a cell suspension.
594 In practice, a ~40% increase is observed for the wild-type AMB-1 after applying a 200
595 mT field (Figure 6a). This increase can be explained by the growth of aligned chain
596 fragments with opposite native polarities within the same cell (Le Nagard et al., 2019). In
597 this case, the application of a strong external field imparts the same polarity to all
598 fragments, increasing the cell's total magnetic moment. A drastically different behavior is
599 observed with the AMB-1 mutant, where the application of a 200 mT field produces an
600 18-fold magnetization increase (Figure 6d). Along with the magnetic behavior assays
601 (C_{mag}), this result indicates a vanishingly small native magnetic moment of the AMB-1
602 mutant, which is compatible with a FC configuration of its looped chains. Overall, these
603 results show that virtually all mutant cells contain looped magnetosome chains.

604 **3.5 Electron holography**

605 Mapping of the magnetic flux in magnetosome chains produced by wild-type AMB-1
606 (Figure 6b,c) indicates that the magnetic moments of individual magnetosomes are nearly
607 parallel to the chain axis, as previously observed (Dunin-Borkowski et al., 1998). In con-
608 trast, necklace structures of the mutant strain display a closed magnetic flux (Figure 6e,f).
609 This configuration has a zero-net magnetic moment, up to small fluctuations due to

asymmetries (e.g., larger crystals on one side of the structure), confirming the origin of the vanishing native magnetic moments of the AMB-1 mutant deduced from magnetic measurements.

3.6 FORC measurements

The FORC diagrams of the wild-type and the mutant AMB-1 (Figure 7) share many similarities with the numerical simulations of single-and double-stranded chains of equi-dimensional crystals, but feature also important differences. The central ridge of wild-type cells extends to the origin and is accompanied by a vertical ridge along $B_c = 0$, located mainly in the lower quadrant. These are the typical signatures of thermal relaxation in systems containing particles close to the lower SD stability limit (Pike et al., 2001; Lanci and Kent, 2018), and has been observed in the growing phase of MTB cultures (Carvallo et al., 2009). In case of single-stranded chains of equidimensional crystals, the lower SD stability limit is comprised between 12 and 17 nm (Newell, 2009) and is compatible with the smallest crystal sizes observed with TEM (Figure 3). The hysteresis squareness ($M_{rs}/M_s = 0.475$) is slightly smaller than expected for single-stranded chains, probably because of a minor superparamagnetic contribution associated with immature chains, as confirmed by electron microscopy (Figure 3). The coercivity distributions obtained from FORC measurements of the wild-type cells (Figure 7c) are unimodal with a peak at 28–30 mT and the right tail extending to a maximum of 60–70 mT. Contrary to the micromagnetic simulations of single-stranded chains of equidimensional magnetosomes (Figure 5a) and to some examples of cultured MTB producing single-stranded chains (e.g., Wang et al., 2015), the coercivity distributions are

632 left-skewed and include a small, non-zero contribution at $B_c = 0$ caused by thermal
633 relaxation.

634 The mutant AMB-1 strain shares the same FORC features (i.e., central ridge, viscous
635 component and rotations of magnetic moments in the applied field), albeit over different
636 field ranges, but also exhibits additional contributions (Figure 7b), consisting of a doublet
637 of positive lobes at (B_c, B_u) ≈ (12, ±8) mT, and a doublet of negative lobes at (B_c, B_u) ≈
638 (25, ±3) mT, almost symmetrically arranged above and below the central ridge. These
639 lobes are the typical hallmark of FC nucleation and annihilation (Egli, 2021), as seen with
640 VO particles (Dumas et al., 2007; Roberts et al., 2017) and small magnetosome clusters
641 produced by the Δ*mamJ* mutant of MSR-1 (Katzmann et al., 2013). The hysteresis loop is
642 constricted (Figure S8), and has a much smaller squareness (Table1, Figure 1) caused by
643 the instability of high-moment magnetic states predicted by micromagnetic simulations of
644 magnetosome rings (Section 3.1). This instability is associated with FORC contributions
645 extending beyond the memory region of the FORC diagram (Figure 7b, left of the dashed
646 lines). Constricted hysteresis loops are typically the result of bimodal coercivity distribu-
647 tions, which, in this case, consist of a main peak at ~2 mT, and a shoulder at ~25 mT
648 (Figure 7d). The main peak of the central ridge, close to the origin, is caused by thermal
649 relaxation of high-moment states, which, as predicted by numerical simulations (Section
650 3.1), are unstable at room temperature. FC nucleation from the negative high-moment
651 state (feature 4 in Figure 7b) contributes additionally to the main peak of the other two
652 coercivity distributions, explaining their larger amplitude with respect to the central
653 ridge. A single mechanism, namely the annihilation of FC states around +25 mT,

explains the existence of a shoulder with similar amplitude in all three coercivity distributions.

About 50% of the high-moment states in looped chains of the AMB-1 mutant possess a stable remanence, as indicated by the portion of the positive lobes above and below the central ridge located within the memory region (i.e., right of the dashed lines in Fig. 7b). This is explainable by the stability of smaller loops with $N \leq 16$ magnetosomes predicted by numerical simulations (Table 2).

4. Discussion

4.1 Distinctive characteristics of the magnetofossil signature

Magnetic assemblages showing coexisting FORC signatures of UNISD particles (central ridge) and non-SD or interacting SD particles (positive contributions above and below the central ridge) were previously interpreted as mixings of several magnetite sources including intact and collapsed magnetofossil assemblages, and non-SD particles of detrital origin (Heslop et al., 2014a; Lascu et al., 2015; Chang et al., 2019). However, mixings of the above-mentioned magnetic sources cannot provide a satisfactory explanation for the elevated hysteresis squareness typical of secondary magnetite in magnetofossil-rich sediments (Ludwig et al., 2013). Our work demonstrates that the magnetic signatures of these sediments can be explained by the sole presence of MTB producing single- and multi-stranded magnetosome chains, as well as specific alterations of these native configurations, such as fold-collapse, which maintain the original strong uniaxial anisotropy. Fold-collapsed chains form a uniform trend with the hysteresis properties of intact chains and UNISD particles (Figure 1), which is characterized by a very limited decrease of the hysteresis squareness ($M_{\mathrm{rs}}/M_{\mathrm{s}} \geq 0.47$), and $B_{\mathrm{cr}}/B_{\mathrm{c}}$ values

677 comprised between ~1.2 and ~1.6, close to the limits for narrow and wide SD coercivity
678 distributions, respectively (Dunlop, 2002).

679 Other putative chain collapse products, such as disordered magnetosome clusters and
680 looped chains, might possess compatible FORC signatures, but lack the elevated
681 hysteresis squareness of systems with stable SD-like remanent states. The hysteresis
682 properties of large clusters of extracted magnetosomes (Kobayashi et al., 2006; Li et al.,
683 2012) follow a trend characterized by a steep M_{rs}/M_s decrease (Figure 1) typical of
684 densely packed synthetic SD magnetite particles (Muxworthy et al., 2003). This decrease
685 is associated with a vertical widening of the FORC function beyond the limits of the
686 memory region (Chen et al., 2007), due to large random internal fields associated with
687 magnetostatic interactions (Muxworthy and Williams, 2005). FORC diagrams of SD
688 particle clusters lack a central ridge (Carvallo et al., 2005); minor central ridge
689 contributions in magnetosome extracts (e.g., Li et al., 2012) are therefore associated with
690 incomplete chain collapse.

691 Micromagnetic simulations of magnetofossil collapse by chain axis randomization
692 (Chang et al., 2019) produce a trend of hysteresis properties that is intermediate between
693 the two cases described above (Figure 1). This trend, which includes the looped chains
694 produced by our mutant AMB-1 as the endmember with lowest squareness, is associated
695 with the intermediate dimensionality of chain loops ($D \approx 2$) and of the partially collapsed
696 chains generated by the random walk algorithm of Harrison and Lascu (2014) ($1 < D <$
697 2), compared to intact or fold-collapsed chains ($D \approx 1$) and dense clusters ($D \approx 3$),
698 respectively. FORC diagrams with non-central ridge contributions and $M_{rs}/M_s \approx 0.5$ are
699 therefore important hallmarks of SD particle systems with a uniaxial anisotropy that is

sufficiently strong to stabilize SD-like remanent states. The only known natural way for secondary SD magnetite particles to develop such a strong uniaxiality is by inheritance of native magnetosome chain structures, which must therefore survive diagenesis without becoming fully randomized. Fold-collapse is one of the possible fates of single-stranded chains that are not immediately stabilized by electrostatic adhesion to other sediment particles. Multi-stranded chains, on the other hand, are expected to be more resistant to mechanical solicitations, due to the staggered magnetosome arrangement, and might survive diagenesis with little structural modifications.

The bell shape of the central ridge coercivity distribution is the second distinctive element of magnetofossil signatures. It is generated by the denucleation of magnetic states with largest switching field: specifically, the high-moment, SD-like state of single-stranded chains, and the low-moment, FC state of multi-stranded chains. Our simulations show that the switching fields of these states tend to form two relatively narrow distributions with medians of ~40–50 mT in the case of equidimensional magnetosomes and ~70–80 mT in the case of prismatic magnetosomes, prior to maghemitization. These distributions are similar to the biogenic components BS and BH discovered in AF demagnetization curves of ARM (Egli, 2004a) and later identified also in the central ridge of magnetofossil-rich sediments (Ludwig et al., 2013; Heslop et al., 2014a). The existence of a minimum uniaxial anisotropy provided by the chain structure ensures that the coercivity distributions of BS and BH are inferiorly limited by a non-zero switching field of ~10 mT (BS) and ~25 mT (BH). This limit is absent in isolated SD particles and in interacting clusters of such particles (Egli, 2021). An interesting counterexample is provided by a mutant MTB producing distant magnetosomes (Wang et al., 2019): in this

723 case, the combined action of magnetic viscosity and lack of strong in-chain magnetostatic
724 interactions shifts the central ridge distribution peak to $B_c = 0$.

725 ARM and the central ridge are expected to have different sensitivities towards single-
726 and double-stranded chains. In case of single-stranded chains, ARM represents the room-
727 temperature thermodynamic equilibrium between two symmetric SD states in the
728 decaying AF field, like in UNISD particles (Egli and Lowrie, 2002). The case of systems
729 featuring two symmetric SD-like states with denucleation field B_{n1} and two symmetric
730 FC states with higher denucleation field B_{n2}, as in double-stranded and fold-collapsed
731 chains, is more complex: once the AF field has decayed below H_{n2} during ARM
732 acquisition, the system becomes trapped into one of the two FC states. In this case, the
733 acquired ARM is a room-temperature thermodynamic equilibrium between two
734 symmetric FC states. This ARM is reset to zero only in AF fields with initial amplitude
735 $\gtrsim B_{n2}$. The similarity between B_{n2} and the switching field of single-stranded chains made
736 of the same type of magnetosomes (Figure 5), yields comparable ARM and central ridge
737 coercivity distributions. However, while the central ridge response is proportional to the
738 mean amplitude of the magnetization jumps associated with FC denucleation, which
739 amounts to ~40% of the saturation moment (M_{cr}/M_s in Table 1), the ARM response is
740 proportional to the remanent moment of FC states, which, in case of identical strands, is
741 nearly zero. Therefore, the ARM of double stranded chains reflects the residual net
742 magnetic moment of asymmetric strands, which is significantly smaller than the
743 saturation moment. FC states are therefore expected to lower the ratio χ_a/M_{rs} between
744 the ARM susceptibility and the saturation remanence. A marked decrease of χ_a/M_{rs} has
745 been observed for the BS and BH components of lake sediments during a eutrophication

746 event and was tentatively attributed to the presence of greigite magnetofossils (Egli,
747 2004a,b). However, greigite-producing MTB appear to have similar magnetic signatures
748 as magnetite-producing MTB (Chen et al., 2014), so that multi-stranded chains are the
749 most likely explanation for χ_a/M_{rs} variations of magnetofossil components.

750 Coercivity distributions obtained from other types of magnetization curves, such as the
751 commonly employed isothermal remanent magnetization (IRM) acquisition (Kruiver et
752 al., 2001), contain contributions from all transitions between magnetic states, which, in
753 the case of multi-stranded chains, include the denucleation of SD-like states in B_{n1}. This
754 additional contribution is easily identifiable as a secondary low-coercivity peak in the
755 case of fold-collapsed chains of equidimensional magnetosomes (Figure 5c), while it
756 merges with the distribution of B_{n2} in the other case, lowering the median field. As a
757 result, coercivity distributions obtained from IRM acquisition curves respond to a larger
758 number of transitions between magnetic states with respect to the central ridge or ARM,
759 yielding less constrained coercivity components that make the identification of BS and
760 BH more difficult or even impossible. More importantly, these coercivity distributions
761 respond also to unstable remanent magnetic states that are switched in arbitrarily small
762 fields, yielding left-skewed curves with non-zero contributions at $B_c = 0$.

763 **4.2 Forward models of magnetofossil FORC signatures**

764 The FORC signature of single-stranded chains is identical to that of UNISD particles:
765 both systems possess only a pair of antisymmetric SD-like states, and the in-field
766 transition between these states produces the central ridge. The transition is preceded by a
767 reversible rotation of magnetic moments, which generates additional FORC contributions
768 in the lower quadrant. The coercivity distributions f_{hys} and f_{cr} associated with in-field

769 magnetization jumps produced by switching between SD-like states are identical and
770 proportional to the coercivity distribution derived from remanent magnetization curves
771 (e.g., f_{dcd}). The small differences between f_{hys} and f_{cr} in Figure 5a,d are due to the
772 numerical method used to isolate the central ridge from other FORC contributions. The
773 difference in amplitude between remanent and in-field coercivity distributions is
774 quantified by M_{cr}/M_{rs}, where M_{cr} is the magnetization associated with the central ridge
775 (Egli et al., 2010). Our micromagnetic simulations yield $M_{cr}/M_{rs} \approx 0.704$ and 0.711 for
776 single-stranded chains of equidimensional and prismatic magnetosomes, respectively,
777 compared to 0.544 for the Stoner-Wohlfarth model (Egli et al., 2010), whereby all
778 estimates do not take thermal activations into account. The higher M_{cr}/M_{rs} values of
779 single-stranded chains are explainable by the fact that reversible magnetic moment
780 rotations is limited mostly to the end magnetosomes, while the magnetic moment of
781 central magnetosomes tend to maintain their remanent state. Non-central ridge
782 contributions in the lower quadrant of the FORC diagram are perfectly antisymmetric
783 with respect to $B_u = -B_c$ and do not contribute to the total magnetization M_{forc} obtained by
784 integrating the FORC function, so that $M_{forc} = M_{cr}$.

785 The FORC diagrams of double-stranded and fold-collapsed chains contain additional
786 non-central ridge contributions originating from transitions between high- and low-
787 moment magnetic states. These contributions create nearly symmetric FORC amplitudes
788 around the central ridge, which contribute to M_{rs} and M_{forc}, but not to M_{cr}. The correspon-
789 ding ratios $M_{cr}/M_{forc} \approx 0.47–0.57$ and $M_{cr}/M_s \approx 0.38–0.42$ are therefore significantly
790 smaller than those of single-stranded chains (Table 3). For comparison, the FORC signa-
791 ture of secondary magnetite particles isolated from a magnetofossil-rich sediment

(Ludwig et al., 2013) is characterized by values of M_{cr}/M_{forc} and M_{cr}/M_s that are intermediate between those of simulated single-stranded and double-stranded or fold-collapsed chains. Mixtures of nearly equal parts of single- and double stranded chains (native and/or fold-collapsed) yield magnetization ratios that are compatible with those of magnetofossils (Table 3). Therefore, a composite FORC diagram has been generated using a mixture of equal amounts of all chain configurations simulated in this work, assuming a 2:1 proportion of equidimensional and prismatic magnetosomes (Figure 8b). This proportion has been chosen to reproduce at best the natural sediment example (Figure 8a). The corresponding FORC diagrams share striking similarities, but also some important differences. Both feature a central ridge, but the coercivity range of simulations is comprised between ~20 and ~130 mT, while the natural central ridge covers also the 0-20 mT range (see Section 4.4).

Other signatures of our composite FORC diagram are qualitatively similar to those of magnetofossil-bearing sediments, including the slight asymmetry between the upper and the lower quadrant, and the abrupt B_c-termination of FC contributions in the upper quadrant. The contour lines of FORC simulation are clearly affected by localized contributions of FC nucleation and annihilation of individual chain endmembers, which are not completely merged into a smooth distribution as in the natural counterpart. Small negative amplitudes above the central ridge are also not completely cancelled. This is understandable considering that simulations were limited to few, well-defined geometries. For instance, single- and multi-stranded chains made of bullet- or tooth-shaped magnetosomes were not included. Multi-stranded chains of bullet-shaped magnetosomes are characterized by similarly elevated hysteresis squareness values as our

double-stranded simulations, with a central ridge peaking at ~60 mT (Li et al., 2010). This intermediate coercivity range fills the gaps between simulated chains of equidimensional and prismatic magnetosomes, making the resulting FORC diagram more similar to that of natural magnetofossils.

4.3 Magnetofossil fingerprints and numerical unmixing

Our numerical simulations show that magnetofossils possess a unique combination of magnetic properties related to the preservation of native or collapsed chain structures with a strong uniaxial anisotropy. This uniaxial anisotropy is at the basis of all magnetic criteria proposed so far for magnetofossil identification, which include (1) the central ridge (Egli et al., 2010; Heslop et al., 2014a), (2) relatively narrow coercivity components not extending to $B_c = 0$ (Egli, 2004a), and (3) ferromagnetic resonance (FMR) spectra with positive anisotropy (Kopp et al., 2006; Charilaou et al., 2011; Kind et al., 2011). An additional criterion discussed in this work is the confinement of FORC contributions within the memory region, which ensures that $M_{cr}/M_s \approx 0.5$ also in case of multi-stranded and fold-collapsed chains. Each of these criteria, if taken singularly, is fulfilled by an equivalent assemblage of isolated SD particles with appropriated equivalent anisotropy, but all known natural examples other than magnetofossils do not fulfill all of them. For instance, titanomagnetite needles in the Tiva Canyon Tuff do possess a central ridge (Berndt et al., 2018), but the associated coercivity distribution and vertical offset are different from those of magnetofossils. In another example (Till et al., 2017), magnetite derived from the inorganic breakdown of nanocrystalline goethite produces FORC diagrams similar to those of magnetofossil-rich sediments, but with a much lower hysteresis squareness. Finally, SD magnetite can form along dislocation lines of silicate

838 minerals, forming “strings of pearls” as documented in ancient zircons (Tang et al.,
839 2018); however, the large irregular particle spacing resulting from this growth process is
840 not expected to yield the narrow coercivity distribution of single-stranded chains.

841 Because natural sediments contain mixtures of magnetite particles with different pri-
842 mary and secondary origins (e.g., Franke et al., 2007; Just et al., 2012; Li et al., 2020),
843 magnetofossil signatures need to be isolated using numerical unmixing methods. Numeri-
844 cal unmixing methods can be divided into parametric ones, which are based on model
845 properties, such as coercivity distribution functions (Kruiver et al., 2001, Egli, 2003), and
846 non-parametric ones, which are fundamentally linked to principal component analysis
847 (PCA), such as non-negative unmixing of remanent magnetization curves (Heslop and
848 Dillon, 2007) and FORC-PCA (Lascu et al., 2015; Harrison et al., 2018). Parametric
849 coercivity analyses are very sensitive to noise and to subtle variations of the shape
850 (skewness) of individual coercivity distributions (Egli, 2003; Zhao et al., 2018).
851 Furthermore, individual coercivity components might be associated with the type of
852 irreversible magnetization changes induced by a particular measurement protocol, rather
853 than distinct types of magnetic particles. This is particularly evident in the case of fold-
854 collapsed chains (Figure 5c), where f_{cr} is described by a single, unimodal distribution,
855 while the other coercivity distributions are bimodal and require two coercivity
856 components for a correct fit. In this case, the analysis of magnetization curves that are
857 selective to specific magnetization processes, such as the central ridge and the AF
858 demagnetization of ARM, helps with the identification of magnetofossil-specific
859 coercivity components.

860 The correct individuation of endmembers in PCA-based unmixing methods is based
861 on the assumption that individual magnetic components possess fixed magnetic
862 properties within the set of analyzed samples. In this case, a single magnetofossil
863 endmember is expected from PCA analyses. More than one endmember is needed to
864 describe magnetofossil signatures that change in time, reflecting, for instance, variable
865 proportions of equidimensional and elongated crystals (Hesse, 1994; Yamazaki and
866 Kawahata, 1998; Wagner et al., 2021), or single- and multi-stranded chains.

867 Our micromagnetic simulations suggest that magnetosome elongation would control
868 mainly the coercivity of magnetofossil endmembers (e.g., the proportion of BS and BH
869 coercivity components), while higher proportions of multi-stranded chains would
870 increase non-central ridge contributions to the FORC diagram. At least two magnetofossil
871 endmembers are required to describe these variations. Splitting between these
872 endmembers is controlled by the PCA covariance matrix, rather than by physical
873 parameters. For instance, variable proportions of single- and multi-stranded chains could
874 be described by the linear combination of a pure central ridge and a pure non-central
875 ridge endmember, instead of the mixed FORC signatures of single- and multi-stranded
876 chains. This might explain FORC-PCA results from the North Atlantic (Channell et al.,
877 2016), where the three identified endmembers include one with the typical FORC
878 signature of detrital magnetite (EM 3 in Fig. 11 of that study), one with a typical UNISD
879 signature consisting of a central ridge, and almost no contributions in the upper quadrant
880 (EM2, ibid), and one that is compatible with non-central ridge contributions from SV
881 magnetite particles or multi-stranded magnetosome chains (EM3, ibid). In this example,
882 the interpretation of the latter endmember is ambiguous; especially when considering that

883 PCA can group the signatures of magnetic components with completely different origins
884 – such as multi-stranded magnetofossils and a fine detrital component SV signature – into
885 a single endmember, if these components co-vary in time. Co-varying concentrations of
886 primary and secondary magnetite particles can be expected if the abundance of
887 magnetofossils is controlled by the flux of nutrients, which, in certain locations, is in turn
888 controlled by primary mineral inputs (e.g., Roberts et al., 2011). Endmembers with
889 characteristics similar to those of the above example are commonly found in marine
890 sediments (Lascu et al., 2015; Yamazaki et al., 2020). FORC-PCA results are also
891 sensitive to the number of principal components and the choice of the endmembers: for
892 example, the FORC signature of a fourth endmember featuring two lobes around the
893 central ridge similar to those of our micromagnetic simulations of double-stranded chains
894 is distributed among the other three endmembers in the case of a three-endmember
895 analysis of the same samples (Fig. 9-10 in Lascu et al., 2015).

896 The ambiguity of numerical unmixing results can be partially overcome by combining
897 numerical methods with particle morphology statistics from TEM observations (Wagner
898 et al., 2021) and with physical or chemical separation techniques, such as the selective
899 dissolution of fine magnetite particles (Ludwig et al., 2013).

900 **4.4 Authigenic magnetite in magnetofossil signatures?**

901 Fe(III)-reducing and Fe(II)-oxidizing bacteria are known to induce the precipitation of
902 magnetite particles that are expected to provide an authigenic contribution to the
903 magnetic signature of sediments affected by iron diagenesis. Ultrafine magnetite particles
904 with broad volume distribution and irregular shapes have been often observed (e.g.,
905 Gibbs-Eggar et al., 1999; Franke et al., 2007; Odlfield, 2007; Li et al., 2020), but their

906 magnetic signature is uncertain, owing to the uncontrolled grain size distribution and the
907 unknown arrangement in the sediment matrix. Magnetite samples produced by these
908 bacteria in the laboratory (Table 1) are characterized by a small squareness (Moskowitz
909 et al., 1993; Carvallo et al., 2008) and the classical FORC signature of strong
910 magnetostatic interactions (Miot et al., 2014). Because of size distribution overlapping
911 with the stable SD range, authigenic magnetite is expected to have a similar preservation
912 potential in geological materials (Roberts et al., 2012) and a magnetic signature that
913 might be confused with that of magnetofossils. Irregularly shaped SD magnetite particles
914 lacking a source of minimum uniaxial anisotropy, for instance by particle elongation or
915 chain arrangement, are expected to produce a broad coercivity distribution with zero-
916 coercivity contributions and median fields of 10-25 mT (Moskowitz et al., 1993).
917 Coercivity components with similar characteristics have been found in freshwater and
918 marine sediments, as well as in soils (EX and P in Egli, 2004a). These components are
919 associated with moderately large χ_a/M_{rs} values typical of non-interacting SD particles
920 (Egli, 2004a), and, in the case of soils, with a central ridge (Geiss et al, 2008; Egli, 2021).
921 Therefore, authigenic magnetite consists, at least in part, of isolated SD particles
922 dispersed in the sediment matrix. The broad grain size distribution of biologically
923 uncontrolled magnetite precipitation (e.g., Liu et al., 2005), which includes SV particles,
924 is expected to yield also FORC signatures typical of non-SD particles, as indeed observed
925 in FORC diagrams of well-developed soils (Egli, 2021). Isolated SD magnetite particles
926 with random deviations from equidimensional shapes are also expected to produce low-
927 coercivity FORC contributions above and below the central ridge (e.g., Fig 51 in Egli,
928 2021), due to the competition between magnetocrystalline and shape anisotropy. Finally,

elevated local iron concentrations might lead to the formation of particle clusters with strong magnetostatic interactions that contribute to the vertical dispersion of the FORC function at low coercivities. Indeed, magnetite encrustation of Fe(III)-reducing or Fe(II)-oxidizing bacteria has been observed in culture (e.g., Miot et al., 2009). For instance, FORC signatures of non-interacting and interacting SD particles not produced by MTB have been identified in organic-rich methanogenic sediments (Ustra et al., 2021). Both non-SD and clustered SD magnetite contributions are expected to lower the hysteresis squareness, and might therefore be distinguishable from pure magnetofossil contributions.

Overall, the SD fraction of well-dispersed authigenic magnetite particles can produce magnetic signatures that might merge continuously with those of magnetofossils over the low-coercivity range. For instance, the low-coercivity FORC-PCA endmembers EM1 and EM2 in red clays from the Pacific Ocean (Yamazaki et al., 2020) provide altogether a signature that is similar to that of the pedogenic enhancement in soils. A low-coercivity component peaking at $B_c = 0$ is also particularly evident in the central ridge of magneto-fossil-bearing ferromanganese crusts formed mainly through biomineralization (Jiang et al., 2020), while being absent in other crusts (Oda et al., 2018). The interpretation of the low-coercivity range (<20 mT) of the central ridge remains uncertain. Short chain frag-ments of 1-3 equant magnetosomes possess significantly lower coercivities than fully developed chains (Chang et al., 2019) and can therefore contribute to the central ridge over this range. It is not known whether such fragments are produced by MTB under natural, slow-growing conditions, or if longer chains are naturally fragmented through adhesion of segments of the same chain to different sediment particles. Overall, the

existence of low-coercivity contributions in the central ridge of most sediments means that a biogenic and an inorganic origin of SD magnetite particles, as postulated by different authors for the Paleocene-Eocene Thermal Maximum, are not mutually exclusive (Kent et al., 2003; Lippert and Zachos, 2007).

4.5 Paleontological and (paleo)environmental implications

Discrimination of single- and multi-stranded chains based on the FORC signatures discussed above are of paleontological interest and could provide a temporal resolution on the evolution of magnetosome formation in MTB. Only bacteria belonging to the ancestral Delta-proteobacteria and Nitrospirae phyla were thought to produce multi-stranded chains of magnetosomes (Deng et al., 2016). However, they have been now identified in the more recent Alpha-proteobacteria and Gamma-proteobacteria phyla (Taoka et al., 2014; Zhang et al., 2017). Therefore, multi-stranded chain configuration has no specific phylogenetic distribution and might instead correspond to an adaptation to specific environments. For instance, single-stranded chain-producing cocci and the multistranded *M. bavaricum* display different responses to a sudden change of the oxygen gradient in sediment (Mao et al., 2014). In MTB, magnetosomes are aligned along cytoskeletal filaments made of actin-like proteins (Müller et al., 2020). Among them, the protein MamK is ubiquitously conserved in all known MTB. Bacteria forming multiple magnetosome chains contain several copies of genes encoding actin-like proteins in addition to MamK (Kolinko et al., 2016). We can thus hypothesize that genetic factors are responsible for multi-stranded chain configurations (Kolinko et al., 2016). They may include gene duplication events (Murat et al., 2010), or horizontal gene transfers (i.e., an exchange of genetic material through direct physical interactions between two organisms)

975 (Monteil et al., 2020). Once the genetic basis of chain configurations (Du et al., 2019) is
976 fully understood, the methodology we describe in this work can be used to provide a
977 temporal constrain on evolutionary events that occurred in one of the oldest and more
978 diverse group of biomineralizing organisms.

979 **4.6 Paleomagnetic implications**

980 Owing to the widespread occurrence of living MTB in the topmost ~10-20 cm of the
981 sedimentary column (Petermann and Bleil, 1993; Flies et al., 2005; Mao et al., 2014) and
982 cell dissolution in the same layer, magnetofossils are expected to contribute to
983 sedimentary records of the Earth magnetic field like other magnetic particles. However,
984 specific differences between the magnetic and mechanical properties of magnetosome
985 chains and other carriers of a natural remanent magnetization (NRM) might affect
986 relative paleointensity records (RPI) of magnetofossil-rich sediments (Larrasoaña et al.,
987 2014; Ouyang et al., 2014; Chen et al., 2017). Although the exact mechanism of NRM
988 acquisition is unknown, it is possible to make some predictions on the influence of chain
989 geometry on the RPI efficiency of magnetofossils on the basis of our findings.

990 Magnetofossils in non-varved sediments are expected to form close to the depth range
991 inhabited by living MTB (Petermann and Bleil, 1993), inside the surface mixed layer
992 (SML). In this case, magnetofossils would undergo the same continuous reorientation
993 process of other remanence carriers, until they are definitively buried below the SML.
994 The resulting NRM has been described as the result of a dynamic equilibrium between
995 (1) the aligning effect of the Earth magnetic field on the net natural magnetic moment of
996 isolated or grouped magnetic particles behaving as rigid mechanical units in the
997 bioturbated sediment (e.g., clusters or inclusions in silicate minerals), and (2) the

rotational diffusion associated with sediment mixing (Egli and Zhao, 2015; Zhao et al., 2016). In this case, the resulting remanent magnetization $M_{\mathrm{nrm}} = M_0 S(m_0 B/\tau_{\mathrm{s}})$ is proportional to the total magnetization M_0 of the remanence carriers in the ideal case of full alignment of their natural magnetic moments, and to a sigmoidal function S, with $S(0) = 0$ and $S(\infty) = 1$, which describes the partial alignment of remanence carriers in the Earth magnetic field B (Egli and Zhao, 2015). In small fields, this partial alignment is proportional to the ratio between the magnetic torque $m_0 B$ of individual remanence carriers with net magnetic moment m_0, and the typical holding torque τ_{s} that resists particle reorientation. Writing $M_0 = c m_0$, where c is the concentration of remanence carriers, gives $M_{\mathrm{nrm}} = c m_0^2 \kappa_{\mathrm{nrm}}$ for the low-field limit of NRM acquisition, with $\kappa_{\mathrm{nrm}} \propto \tau_{\mathrm{s}}^{-1}$ being a coefficient that describes the mechanical alignment efficiency of the remanence carriers in sediments with specific mechanical properties.

RPI records are obtained by normalizing M_{nrm} with a laboratory magnetization M_{lab} assumed to be proportional to M_0. In this case, $M_{\mathrm{lab}} = c m_{\mathrm{lab}}$, with m_0 being the mean magnetic moment component along the applied magnetic field, acquired by the remanence carriers during the acquisition of a laboratory magnetization. The normalized NRM is finally given by $R = \kappa_{\mathrm{nrm}} m_0^2 / m_{\mathrm{lab}} B$. As expected for valid RPI normalizations, R does not depend on the concentration of remanence carriers. Furthermore, a fixed magnetic mineralogy yields a constant m_0^2/m_{lab}, so that R is proportional to B.

Each magnetic component contributing to the NRM is expected to possess a specific m_0^2/m_{lab} value related to its magnetic properties, and a specific κ_{nrm} that reflects its mechanical properties. Accordingly, sediments containing variable proportions of two or more magnetic components (e.g., detrital and biogenic), yield RPI records that contain an

unwanted environmental modulation caused by variations of $\kappa_{\mathrm{nrm}} m_0^2/m_{\mathrm{lab}}$ within the limit values of the individual components (Fabian and Leonhardt, 2009). The role of m_0^2/m_{lab} can be investigated by inspecting selected categories of remanence carriers. For instance, the natural magnetic moment of silicate minerals containing $n \lesssim 50$ SD magnetic inclusions is proportional to the sum of n randomly oriented vectors, which yields $m_0 \approx m_{\mathrm{SD}}\sqrt{8n/3\pi}$, where m_{SD} is the mean magnetic moment of individual SD particles (Heslop et al., 2014b). For comparison, intact chains of n magnetosomes are characterized by $m_0 = m_{\mathrm{SD}} n$, while fold-collapsed chains have a much smaller native moment $m_0 = m_{\mathrm{SD}}\delta n$, where δn is the mean absolute difference between the number of magnetosomes in the two strands (e.g., $\delta n = 0$ for a chain that is folded exactly in the middle). A similar reasoning can be applied to the estimation of magnetic moments produced by the ARM and IRM magnetizations commonly used as RPI normalizers (Table 4).

Magnetofossil RPI values obtained with the above magnetic moment estimates display different degrees of sensitivity to the chain structure. If IRM is used as normalizer, similar RPI estimates are expected for intact single- and multistranded chains, since they carry a saturated magnetic moment in their native state and after application of a saturating IRM. Fold-collapsed chains, on the other hand, have a small net native moment, making them inefficient NRM carriers. If ARM is used as a normalizer, intact double stranded chains are expected to yield larger RPI values than intact single-stranded chains, because the ARM sets multistranded chains in a FC state with low magnetic moment (See Section 4.1). In case of comparable mechanical alignment efficiencies (κ_{nrm}), intact magnetofossils are expected to possess larger RPI efficiencies relative to

silicate minerals containing SD magnetite inclusions with the same saturation moment, as reported by Ouyang et al. (2014) and Chen et al. (2017), because the magnetic moments of individual crystals add arithmetically to the native net moment, instead of randomly.

5. Conclusions

Rock and sediment magnetism methodologies have been extensively used for the search and identification of magnetofossils. The central ridge observed during FORC analyses was established as a distinctive feature of the strong uniaxial anisotropy of isolated magnetosome chains. Our findings show that intact multi-stranded and fold-collapsed chains can generate additional signatures in FORC diagrams through the nucleation and annihilation of FC magnetic states while maintaining high hysteresis squareness (M_{rs}/M_s). FC magnetic states in multi-stranded chains, which can be described by individual strands possessing opposed magnetic polarities, are similar to FC states observed in small magnetosome clusters and looped magnetosome chains forming after cell dissolution in aqueous solutions, which might serve as term of comparison for diagenetic chain collapse in sediment. However, these artificial magnetosome structures are characterized by a significantly lowered hysteresis squareness that is not observed in magnetofossil-rich sediments. Micromagnetic calculations show that native multi-stranded chains and fold-collapsed chains feature stable SD states with large magnetic moments and the same hysteresis squareness of intact single-stranded chains. This stability, which has been confirmed experimentally in the case of native chains (Hanzlik et al. 2002; Thomas et al., 2008), originates from the strong uniaxial anisotropy of such structures and explains the coexistence of (1) magnetic signatures typical for systems of isolated SD particles and single-stranded magnetosome chains (central ridge and

1067 $M_{rs}/M_s \approx 0.5$), and (2) signatures typical of SD particle systems with random
1068 magnetostatic interactions (non-central-ridge contributions in the FORC diagram).

1069 Full chain collapse leading to a complete loss of the original structure is likely
1070 prevented by the electrostatic adhesion of magnetosomes to sediment particles.
1071 Therefore, the strong uniaxial anisotropy of intact and fold-collapsed magnetosome
1072 chains appears to be a key feature for the preservation of a unique magnetic signature of
1073 magnetofossils, which, besides the elevated hysteresis squareness and a central ridge,
1074 includes two coercivity components (BS and BH in Egli, 2004a) with inferiorly limited,
1075 Gaussian-like switching field distributions distinct from those of isolated or clustered SD
1076 magnetite particles. Our micromagnetic models suggest that the low-coercivity portion of
1077 the central ridge of natural sediments (Figure 8) likely represents the contribution of
1078 isolated SD particles of authigenic origin. ARM is another key parameter of
1079 magnetofossil fingerprints: its coercivity distribution is similar to that of the central ridge,
1080 but, unlike to the central ridge, it is more selective towards single-stranded chains.

1081 Preservation of a distinctive magnetofossil fingerprint, as demonstrated in our work,
1082 is pivotal for the interpretation of the origin of secondary SD magnetite particles in sedi-
1083 ments, since this fingerprint is the only practical mean for verifying, in a quantitative
1084 manner, the existence of isolated chain-like structures of SD magnetite particle as the
1085 most essential magnetofossil identification criterion. The detailed characteristics of
1086 magnetofossil fingerprints depend on the relative abundances of equidimensional and
1087 elongated magnetosomes, which affect the coercivity distribution, and on the relative
1088 abundances single- and multi-stranded chains, which affect the fraction of magnetic
1089 remanence carried by the central ridge. Magnetosome shape and chain structure reflect

environmental conditions controlling the growth of different MTB strains. Therefore, detailed magnetofossil records obtained with high-resolution FORC measurements, combined with statistically significant TEM observations, will provide novel methodologies to discriminate distinct populations of ancient MTB and improve our understanding of paleomagnetic and environmental records of magnetofossil-rich sediments.

Acknowledgements. AK and MA are supported by grants through the National Science Foundation (1504681) and National Institutes of Health (R35GM127114). MA is supported by grant through the *Fondation pour la Recherche Médicale* (ARF201909009123). The research leading to these results has received funding from the European Union Horizon 2020 research and innovation program under grant agreement No. 823717 – ESTEEM3. The authors acknowledge the French National Research Agency under the "Investissement d'Avenir" program reference No. ANR-10-EQPX-38-01 and the "Conseil Régional Midi-Pyrénées" and the European FEDER for financial support within the CPER program. This work was also supported by the international associated laboratory M^2OZART. All data generated in this work are available on https://figshare.com/collections/Magnetic_Signatures_of_Magnetofossils/5579547.

References

Abreu, N., Mannoubi, S., Ozyamak, E., Pignol, D., Ginet, N., & Komeili, A. (2014). Interplay between two bacterial actin homologs, MamK and MamK-like, is required for the alignment of magnetosome organelles in *Magnetospirillum magneticum* AMB-1. *Journal of Bacteriology*, *196*, 3111–3121. https://doi.org/10.1128/JB.01674-14.

Amor, M., Mathon, F. P., Monteil, C. L., Busigny, V., & Lefevre, C. T. (2020). Iron-biomineralizing organelle in magnetotactic bacteria: function, synthesis and preservation in ancient rock samples. *Environmental Microbiology*, *22*, 3611–3632. https://doi.org/10.1111/1462-2920.15098.

Berndt, T. A., Chang, L. & Pei, Z. (2020). Mind the gap: Towards a biogenic magnetite palaeoenvironmental proxy through an extensive finite-element micromagnetic simulation, *Earth and Planetary Science Letters*, *532*, 116010, https://doi.org/10.1016/j.epsl.2019.116010.

Berndt, T. A., Chang, L., Wang, S., & Badejo, S. (2018). Time-asymmetric FORC diagrams: A new protocol for visualizing thermal fluctuations and distinguishing magnetic mineral mixtures. *Geochemistry Geophysics Geosystems*, *19*, 3056–3070. https://doi.org/10.1029/2018GC007669.

Carvallo, C., Dunlop, D. J., & Özdemir, Ö. (2005). Experimental comparison of FORC and remanent Preisach diagrams. *Geophysical Journal International*, *162*, 747–754. https://doi.org/10.1111/j.1365-246X.2005.02688.x.

Carvallo, C., Hickey, S., Faivre, D., & Menguy, N. (2009). Formation of magnetite in *Magnetospirillum gryphiswaldense* studied with FORC diagrams, *Earth Planets Space*, *61*, 143–150, https://doi.org/10.1186/BF03352894.

Carvallo, C., Sainctavit, P., Arrio, M.-A., Menguy, N., Wang, Y., Ona-Nguema, G., & Brice-Profeta, S. (2008). Biogenic vs. abiogenic magnetite nanoparticles: a XMCD study, *American Mineralogist*, *93*, 880–885, https://doi.org/10.2138/am.2008.2713.

Chang, L., Harrison, R. J., & Berndt, T. A. (2019). Micromagnetic simulation of magnetofossils with realistic size and shape distributions: Linking magnetic proxies with nanoscale observations and implications for magnetofossil identification. *Earth and Planetary Science Letters*, *527*, 115790, https://doi.org/10.1016/j.epsl.2019.115790.

Chang, L., Harrison, R. J., Zeng, F., Berndt, T. A., Roberts, A. P., Heslop, D., & Zhao, X. (2018). Coupled microbial bloom and oxygenation decline recorded by magnetofossils during the Paleocene-Eocene thermal maximum, *Nature Communications*, *9*, 4007, https://doi.org/10.1038/s41467-018-06472-y.

Chang, L., Roberts, A. P., Heslop, D., Hayashida, A., Li, J., Zhao, X., et al. (2016). Widespread occurrence of silicate-hosted magnetic mineral inclusions in marine sediments and their contribution to paleomagnetic recording. *Journal of Geophysical Research: Solid Earth*, *121*, 8415–8431, https://doi.org/10.1002/2016JB013109.

Channell, J. E. T., Harrison, R. J., Lascu, I., McCave, I. N., Hibbert, F. D., & Austin, W. E. N. (2016). Magnetic record of deglaciation using FORC-PCA, sortable-silt grain size, and magnetic excursion at 26 ka, from the Rockall Trough (NE Atlantic). *Geochemistry Geophysics Geosystems*, *17*, 1823–1841. https://doi.org/10.1002/2016GC006300.

Charilaou, M., Winklhofer, M., & Gehring, A. U. (2011). Simulation of ferromagnetic resonance spectra of linear chains of magnetite nanocrystals, *Journal of Applied Physics*, *109*, 093903, https://doi.org/10.1063/1.3581103.

Chen, A. P., Berounsky, V. M., Chan, M. K., Blackford, M. G., Cady, C., Moskowitz, B. M., et al. (2014). Magnetic properties of uncultivated magnetotactic bacteria and their contribution to a stratified estuary iron cycle. *Nature Communications*, *5*, 4797, https://doi.org/10.1038/ncomms5797.

Chen, A. P., Egli, R., & Moskowitz, B. M. (2007). First-order reversal curve (FORC) diagrams of natural and cultured biogenic magnetic particles, *Journal of Geophysical Research*, *112*, B08S90, https://doi.org/10.1029/2006JB004575.

Chen, L., Heslop, D., Roberts, A. P., Chang, L., Zhao, X., McGregor, H. V., Marino, G., Rodriguez-Sanz, L., Rohling, E. J., & Pälike, H. (2017). Remanence acquisition efficiency in biogenic and detrital magnetite and recording of geomagnetic paleo-intensity, *Geochemistry Geophysics Geosystems*, *18*, 1435–1450, https://doi.org/10.1002/2016GC006753.

Dearing, J. A., Hannam, J. A., Anderson, A. S., & Wellington, E. M. H. (2001). Magnetic, geochemical and DNA properties of highly magnetic soils in England, *Geophysical Journal International*, *144*, 183–196, https://doi.org/10.1046/j.0956-540X.2000. 01312.x.

Deng, A., Lin, W., Shi, N., Wu, J., Sun, Z., Sun, Q., et al. (2016). In vitro assembly of the bacterial actin protein MamK from 'Candidatus Magnetobacterium casensis' in the phylum Nitrospirae. *Protein & Cell*, *7*, 267–280. https://doi.org/10.1007/s13238-016-0253-x.

Dobeneck, T., Petersen, N., & Vali, H. (1987). Bacterial magnetofossils (in German), *Geowissenschaften in unserer Zeit*, *5*, 27–35.

Draper, O., Byrne, M. E., Li, Z., Keyhani, S., Barrozo, J. C., Jensen, G., & Komeili, A. (2011). MamK, a bacterial actin, forms dynamic filaments in vivo that are regulated by the acidic proteins MamJ and LimJ. *Molecular Microbiology*, *82*, 342–354, https://doi.org/10.1111/j.1365-2958.2011.07815.x.

Du, H., Zhang, W., Zhang, W., Zhang, W., Pan, H., Pan, Y., Bazylinski, D. A., Wu, L.-F., Xiao, T., Lin W. (2019). Magnetosome gene duplication as an important river in the evolution of magnetotaxis in the *Alphaproteobacteria*. *mSystems*, *4*, e00315-19, https://doi.org/10.1128/mSystems.00315-19.

Dumas, R. K., Li, C.-P., Roshchin, I. V., Schuller, I. K., & Liu, K. (2007). Magnetic fingerprints of sub-100 nm Fe dots. *Physical Review B*, *75*, 134405, https://doi.org/10.1103/PhysRevB.75.134405.

Dunin-Borkowski, R. E., Kasama, T., Wei, A., Tripp, S. L., Hytch, M. J., Snoeck, E., Harrison, R. J., & Putnis, A. (2004). Off-axis electron holography of magnetic nanowires and chains, rings, and planar arrays of magnetic nanoparticles, *Microscopy Research and Technique*, *64*, 390–402, https://doi.org/10.1002/jemt.20098.

Dunin-Borkowski, R. E., McCartney, M. R., Frankel, R. B., Bazylinski, D. A., Posfai, M., & Buseck, P. R. (1998). Magnetic microstructure of magnetotactic bacteria by electron holography. *Science*, *282*, 1868–1870, https://doi.org/10.1126/science.282.5395.1868.

Dunlop, D. J. (2002). Theory and application of the Day plot (M_{rs}/M_s versus H_{cr}/H_c) 1, Theoretical curves and tests using titanomagnetite data, *Journal of Geophysical Research: Solid Earth*, *107*, 2056, https://doi.org/10.1029/2001JB000486.

Egli, R. (2003). Analysis of the field dependence of remanent magnetization curves, *Journal of Geophysical Research: Solid Earth*, *108*, 2081, https://doi.org/10.1029/2002JB002023.

1201 Egli, R. (2004a). Characterization of Individual Rock Magnetic Components by Analysis
1202 of Remanence Curves, 1. Unmixing Natural Sediments. *Studia Geophysica et*
1203 *Geodaetica*, *48*, 391–446, https://doi.org/10.1023/B:SGEG.0000020839.45304.6d.

1204 Egli, R. (2004b). Characterization of individual rock magnetic components by analysis of
1205 remanence curves, 3. Bacterial magnetite and natural processes in lakes, *Physics and*
1206 *Chemistry of the Earth*, *29*, 869–884, https://doi.org/10.1016/j.pce.2004.03.010.

1207 Egli, R. (2013). VARIFORC: An optimized protocol for calculating non-regular first-
1208 order reversal curve (FORC) diagrams. *Global and Planetary Change*, *110*, 302–320.
1209 https://doi.org/10.1016/j.gloplacha.2013.08.003.

1210 Egli, R. (2021). Magnetic characterization of geologic materials with first-order reversal
1211 curves, in V. Franco and B. Dodrill (Eds.): *Magnetic Measurement Techniques for*
1212 *Materials Characterization*, Springer, https://doi.org/10.1007/978-3-030-70443-8.

1213 Egli, R., Chen, A. P., Winklhofer, M., Kodama, K. P., & Horng, C.-S. (2010). Detection
1214 of noninteracting single domain particles using first-order reversal curve diagrams.
1215 *Geochemistry Geophysics Geosystems*, *11*, Q01Z11, https://doi.org/10.1029/
1216 2009GC002916.

1217 Egli, R., & Lowrie, W. (2002). Anhysteretic remanent magnetization of fine magnetic
1218 particles, *Journal of Geophysical Research: Solid Earth*, *107*, 2209, https://doi.org/
1219 10.1029/2001JB000671.

1220 Egli, R., Florindo, F., & Roberts, A. (2013). Introduction to "Magnetic iron minerals in
1221 sediments and their relation to geologic processes, climate, and the geomagnetic
1222 field". *Global and Planetary Change*, *110*, 259–263,
1223 https://doi.org/10.1016/j.gloplacha.2013. 10.009.

1224 Egli, R., & Zhao, X. (2014). Natural remanent magnetization acquisition in bioturbated
1225 sediment: General theory and implications for relative paleointensity reconstructions,
1226 *Geochemistry Geophysics Geosystems*, *16*, 995–1016, https://doi.org/10.1002/
1227 2014GC005672.

1228 Evans, M. E., & F. Heller (2003). *Environmental Magnetism: Principles and*
1229 *Applications of Enviromagnetics*, Academic Press.

1230 Fabian, K., & Leonhardt, R. (2009). Records of paleomagnetic field variations, in K.-H.
1231 Glassmeier et al. (eds.), *Geomagnetic Field Variations*, Advances in Geophysical and
1232 Environmental Mechanics and Mathematics, Springer, 65–106,
1233 https://doi.org/10.1007/ 978-3-540-76939-2_3.

1234 Fabian, K., & Shcherbakov, V. (2018). Energy barriers in three-dimensional micro-
1235 magnetic models and the physics of thermoviscous magnetization, *Geophysical*
1236 *Journal International*, *215*, 314–324, https://doi.org/10.1093/gji/ggy285.

1237 Faivre, D., Agrinier, P., Menguy, N., Zuddas, P., Pachana, K., Gloter, A., Laval, J.-Y., &
1238 Guyot, F. (2004). Mineralogical and isotopic properties of inorganic nanocrystalline
1239 magnetites, *Geochimica et Cosmochimica Acta*, *68*, 4395–4403, https://doi.org/
1240 10.1016/j.gca.2004.03.016.

1241 Flies, C. B., Jonkers, H. M., de Beer, D., Bosselmann, K., Bottcher, M. E., & Schuler, D.
1242 (2005). Diversity and vertical distribution of magnetotactic bacteria along chemical
1243 gradients in freshwater microcosms. *FEMS Microbiology Ecology*, *52*, 185–195.
1244 https://doi.org/10.1016/j.femsec.2004.11.006.

1245 Fortin, D., & Langley, S. (2005). Formation and occurrence of biogenic iron-rich
1246 minerals. *Earth-Science Reviews*, *72*, 1–19,
1247 https://doi.org/10.1016/j.earscirev.2005.03.002.

1248 Franke, C., von Dobeneck, T., Drury, M. R., Meelijk, J. D., & Dekkers, M. (2007).
1249 Magnetic petrology of equatorial Atlantic sediments: Electron microscopy results and
1250 their implications for environmental magnetic interpretation, *Paleoceanography*, *22*,
1251 PA4207, https://doi.org/10.1029/2007PA001442.

1252 Galindo-Gonzalez, C., Feinberg, J. M., Kasama, T., Cervera Gontard, L., Pósfai, M.,
1253 Kósa, I., Duran, J. D. G., Gil, J. E., Harrison, R. J., & Dunin-Borkowski, R. E. (2009).
1254 Magnetic and microscopic characterization of magnetite nanoparticles adhered to clay
1255 surfaces, *American Mineralogist*, *94*, 1120–1129, https://doi.org/10.2138/am.2009.
1256 3167.

1257 Gatel, C., Dupuy, J., Houdellier, F., & Hÿtch, M. J. (2018). Unlimited acquisition time in
1258 electron holography by automated feedback control of transmission electron micro-
1259 scope. *Applied Physics Letters*, *113*, 133102, https://doi.org/10.1063/1.5050906.

1260 Geiss, C. E., Egli, R., & Zanner, C. W. (2008). Direct estimates of pedogenic magnetite
1261 as a tool to reconstruct past climates from buried soils. *Journal of Geophysical*
1262 *Research: Solid Earth*, *113*, B11102, https://doi.org/10.1029/2008JB005669.

Gibbs-Eggar, Z., Jude, B., Dominik, J., Loizeau, J.-L., & Oldfield, F. (1999). Possible evidence for dissimilatory bacterial magnetite dominating the magnetic properties of recent lake sediments, *Earth and Planetary Science Letters*, *168*, 1–6, https://doi.org/10.1016/S0012-821X(99)00054-0.

Golden, D. C., Ming, D. W., Morris, R. V., Brearley, A. J., Lauer, H. V., Treiman, A. H., Zolensky, M. E., Schwandt, C. S., Lofgren, G. E., & McKay, G. A. (2004). Evidence for exclusively inorganic formation of magnetite in Martian meteorite ALH84001. *American Mineralogist*, *89*, 681–695, https://doi.org/10.2138/am-2004-5-602.

Hanzlik, M., Winklhofer, M., & Petersen, N. (2002). Pulsed-field-remanence measurements on individual magnetotactic bacteria. *Journal of Magnetism and Magnetic Materials*, *248*, 258–267, https://doi.org/10.1016/S0304-8853(02)00353-0.

Harada, K., Tonomura, A., Togawa, Y., Akashi, T., & Matsuda, T. (2004). Double-biprism electron interferometry. *Applied Physics Letters*, *84*, 3229–3231, https://doi.org/ 10.1063/1.1715155.

Harrison, R. J., & Lascu, I. (2014). FORCulator: A micromagnetic tool for simulating first-order reversal curve diagrams. *Geochemistry, Geophysics, Geosystems*, *15*, 4671–4691, https://doi.org/10.1002/2014GC005582.

Harrison, R. J., Muraszko, J., Heslop, D., Lascu, I., Muxworthy, A. R., & Roberts, A. P. (2018). An improved algorithm for unmixing first-order reversal curve diagrams using principal component analysis, *Geochemistry Geophysics Geosystems*, *19*, 1595–1610, https://doi.org/10.1029/2018GC007511.

Hendriksen, P. V., Christiansen, G., & Mørup, G. (1994). Magnetization reversal in chain-like clusters of interacting particles, *Journal of Magnetism and Magnetic Materials*, *132*, 207–218, https://doi.org/10.1016/0304-8853(94)90315-8.

Heslop, D., & Dillon, M. (2007). Unmixing magnetic remanence curves without a priori knowledge, *Geophysical Journal International*, *170*, 556–566, https://doi.org/10.1111/j.1365-246X.2007.03432.x.

Heslop, D., Roberts, A. P., & Chang, L. (2014a). Characterizing magnetofossils from first-order reversal curve (FORC) central ridge signatures. *Geochemistry Geophysics Geosystems*, *15*, 2170–2179, https://doi.org/10.1002/2014GC005291.

Heslop, D., Roberts, A. P., & Hawkins, R. (2014b). A statistical simulation of magnetic particle alignment in sediments, *Geophysical Journal International*, *197*, 828–837, https://doi.org/10.1093/gji/ggu038.

Hesse, P. P. (1994). Evidence for bacterial palaeoecological origin of mineral magnetic cycles in oxic and sub-oxic Tasman Sea sediments. *Marine Geology*, *117*, 1–17, https://doi.org/10.1016/0025-3227(94)90003-5.

Housen, B. A., & Moskowitz, B. M. (2006). Depth distribution of magnetofossils in near-surface sediment from the Blake/Bahama Outer Ridge, western North Atlantic Ocean, determined by low-temperature magnetism, *Journal of Geophysical Research*, *111*, G01005, https://doi.org/10.1029/2005JG000068.

Jiang, X. D., Zhao, X., Chou, Y. M., Liu, Q. S., Roberts, A. P., Ren, J. B., Sun, X., M., Li, J. H., Tang, X., Zhao, X. Y., & Wang, C. C. (2020). Characterization and quantification of magnetofossils within abyssal manganese nodules from the western Pacific Ocean and implications for nodule formation, *Geochemistry Geophysics Geosystems*, *21*, e2019GC008811, https://doi.org/10.1029/2019GC008811.

Jovane, L., Florindo, F., Bazylinski, D. A., & Lins, U. (2012). Prismatic magnetite magnetosomes from cultivated Magnetovibrio blakemorei strain MV-1: a magnetic fingerprint in marine sediments?, *Environmental Microbiology Reports*, *4*, 664–668, https://doi.org/10.1111/1758-2229.12000.

Just, J., Dekkers, M. J., von Dobeneck, T., van Hoesel, A., & Bickert, T. (2012). Signatures and significance of aeolian, fluvial, bacterial and diagenetic magnetic mineral fractions in Late Quaternary marine sediments off Gambia, NW Africa, *Geochemistry Geophysics Geosystems*, *13*, Q0AO02, https://doi.org/10.1029/2012GC004146.

Katzmann, E., Eibauer, M., Lin, W., Pan, Y., Plitzko, J. M., & Schüler, D. (2013). Analysis of Magnetosome Chains in Magnetotactic Bacteria by Magnetic Measurements and Automated Image Analysis of Electron Micrographs. *Applied and Environmental Microbiology*, *79*, 7755–7762, https://doi.org/10.1128/AEM.02143-13.

Kent, D. V., Cramer, B. S., Lanci, L., Wang, D., Wright, J. D., & Van der Voo, R. (2003). A case for a comet impact trigger for the Paleocene/Eocene thermal maximum and carbon isotope excursion, *Earth and Planetary Science Letters*, *211*, 13–26, https://doi.org/10.1016/S0012-821X(03)00188-2.

1325 Kiani, B., Faivre, D. & Klumpp, S. (2015). Elastic properties of magnetosome chains,
1326 *New Journal of Physics*, *17*, 043007, https://doi.org/10.1088/1367-2630/17/4/043007.

1327 Kiani, B., Faivre, D. & Klumpp, S. (2018). Self-organization and stability of
1328 magnetosome chains — A simulation study, PLOS One, 13, e0190265,
1329 https://doi.org/10.1371/ journal.pone.0190265.

1330 Kind, J., Gehring, A. U., Winklhofer, M., & Hirt, A. M. (2011). Combined use of
1331 magnetometry and spectroscopy for identifying magnetofossils in sediments,
1332 *Geochemistry Geophysics Geosystems*, *12*, Q08008,
1333 https://doi.org/10.1029/2011GC003633.

1334 Kobayashi, A., Kirschvink, J. L., Nash, C. Z., Kopp, R. E., Sauer, D. A., Bertani, L. E., et
1335 al. (2006). Experimental observation of magnetosome chain collapse in magnetotactic
1336 bacteria: Sedimentological, paleomagnetic, and evolutionary implications. *Earth and*
1337 *Planetary Science Letters*, *245*, 538–550, https://doi.org/10.1016/j.epsl.2006.03.041.

1338 Kolinko, S., Richter, M., Gloeckner, F.-O., Brachmann, A., & Schueler, D. (2016).
1339 Single-cell genomics of uncultivated deep-branching magnetotactic bacteria reveals a
1340 conserved set of magnetosome genes. *Environmental Microbiology*, *18*, 21–37,
1341 https://doi.org/10.1111/1462-2920.12907.

1342 Komeili, A., Zhuo, L., Newmann, D. K., & Jensen, G. J. (2006). Magnetosomes are cell
1343 membrane invaginations organized by the actin-like protein MamK, *Science*, *311*,
1344 242–245, https://doi.org/10.1126/science.1116804.

1345 Kopp, R. E., & Kirschvink, J. L. (2008). The identification and biogeochemical
1346 interpretation of fossil magnetotactic bacteria. *Earth-Science Reviews*, *86*, 42–61,
1347 https://doi.org/10.1016/j.earscirev.2007.08.001.

1348 Kopp, R. E., Nash, C. Z., Kobayashi, A., Weiss, B. P., Bazylinski, D. A., & Kirschvink,
1349 J. L. (2006). Ferromagnetic resonance spectroscopy for assessment of magnetic
1350 anisotropy and magnetostatic interactions: A case study of mutant magnetotactic
1351 bacteria, *Journal of Geophysical Research*, *111*, B12S25, https://doi.org/10.1029/
1352 2006JB004529.

1353 Kopp, R. E., Raub, T. D., Schumann, D., Vali, H., Smirnov, A. V., & Kirschvink, J. L.
1354 (2007). Magnetofossil spike during the Paleocene-Eocene thermal maximum:
1355 Ferromagnetic resonance, rock magnetic, and electron microscopy evidence from
1356 Ancora, New Jersey, United States. *Paleoceanography*, *22*, PA4103, https://doi.org/
1357 10.1029/2007PA001473.

1358 Kruiver, P. P., Dekkers, M. J., & Heslop, D. (2001). Quantification of magnetic
1359 coercivity componets by the analysis of acquisition curves of isothermal remanent
1360 magnetization. *Earth and Planetary Science Letters*, *189*, 269–276,
1361 https://doi.org/10.1016/S0012-821X(01)00367-3.

1362 Lanci, L., & Kent, D. V. (2018). Forward modeling of thermally activated single-domain
1363 magnetic particles applied to first-order reversal curves. *Journal of Geophysical*
1364 *Research: Solid Earth*, *123*, 3287–3300. https://doi.org/10.1002/2018JB015463.

1365 Larrasoaña, J. C., Liu, Q., Hu, P., Roberts, A. P., Mata, P., Civis, J., et al. (2014).
1366 Paleomagnetic and paleoenvironmental implications of magnetofossil occurrences in
1367 late Miocene marine sediments from the Guadalquivir Basin, SW Spain. *Frontiers in*
1368 *Microbiology*, *5*, 71, https://doi.org/10.3389/fmicb.2014.00071.

1369 Lascu, I., Einsle, J. F., Ball, M. R., & Harrison, R. J. (2018). The vortex state in geologic
1370 materials: A micromagnetic perspective. *Journal of Geophysical Research: Solid*
1371 *Earth*, *123*, 7285–7304, https://doi.org/10.1029/2018JB015909.

1372 Lascu, I., Harrison, R. J., Li, Y., Muraszko, J. R., Channell, J. E. T., Piotrowski, A. M., &
1373 Hodell, D. A. (2015). Magnetic unmixing of first-order reversal curve diagrams using
1374 principal component analysis. *Geochemistry Geophysics Geosystems*, *16*, 2900–2915,
1375 https://doi.org/10.1002/2015GC005909.

1376 Lefèvre, C. T., Pósfai, M., Abreu, F., Lins, U., Frankel, R. B., & Bazylinski, D. A.
1377 (2011). Morphological features of elongated-anisotropic magnetosome crystals in
1378 magnetotactic bacteria of the Nitrospirae phylum and the Deltaproteobacteria class.
1379 *Earth and Planetary Science Letters*, *312*, 194–200,
1380 https://doi.org/10.1016/j.epsl.2011.10.003.

1381 Le Nagard, L., Zhu, X., Yuan, H., Benzerara, K., Bazylinski, D. A., Fradin, C., et al.
1382 (2019). Magnetite magnetosome biomineralization in Magnetospirillum magneticum
1383 strain AMB-1: A time course study. *Chemical Geology*, *530*, 119348,
1384 https://doi.org/10.1016/ j.chemgeo.2019.119348.

1385 Lewis, G. R., Loudon, J. C., Tovey, R., Chen, Y.-H., Roberts, A. P., Harrison, R. J.,
1386 Midgley, P. A., & Ringe, E. (2020). Magnetic vortex states in toroidal iron oxide
1387 nanoparticles: combining micromagnetics with tomography. *Nano Letters*, *20*, 7405–
1388 7412, https://doi.org/10.1021/acs.nanolett.0c02795.

Li, J., Liu, Y., Liu, S., Roberts, A. P., Pan, H., Xiao, T., & Pan, Y. (2020). Classification of a complexly mixed magnetic mineral assemblage in Pacific Ocean surface sediment by electron microscopy and supervised magnetic unmixing. *Frontiers in Earth Science*, *8*, 609058, https://doi.org/10.3389/feart.2020.609058.

Li, J., Menguy, N., Gatel, C., Boureau, V., Snoeck, E., Patriarche, G., et al. (2015). Crystal growth of bullet-shaped magnetite in magnetotactic bacteria of the Nitrospirae phylum. *Journal of the Royal Society Interface*, *12*, 20141288, https://doi.org/10.1098/rsif.2014.1288.

Li, J., Pan, Y., Liu, Q., Yu-Zhang, K., Menguy, N., Che, R., et al. (2010). Biomineralization, crystallography and magnetic properties of bullet-shaped magnetite magnetosomes in giant rod magnetotactic bacteria. *Earth and Planetary Science Letters*, *293*, 368–376, https://doi.org/10.1016/j.epsl.2010.03.007.

Li, J., Wu, W., Liu, Q., & Pan, Y. (2012). Magnetic anisotropy, magnetostatic interactions and identification of magnetofossils. *Geochemistry Geophysics Geosystems*, *13*, Q10Z51, https://doi.org/10.1029/2012GC004384.

Lin, W., Paterson, G. A., Zhu, Q., Wang, Y., Kopylova, E., Li, Y., et al. (2017). Origin of microbial biomineralization and magnetotaxis during the Archean. *Proceedings of the National Academy of Sciences of the United States of America*, *114*, 2171–2176, https://doi.org/10.1073/pnas.1614654114.

Lins, U. & Farina, M. (2004). Magnetosome chain arrangement and stability in magnetotactic cocci, *Antoine van Leeuwenhoek*, *85*, 335–341, https://doi.org/10.1023/B:ANTO.0000020393.71843.b0.

Lippert, P. C., & Zachos, J. C. (2007). A biogenic origin for anomalous fine-grained magnetic material at the Paleocene-Eocene boundary at Wilson Lake, New Jersey. *Paleoceanography*, *22*, PA4104, https://doi.org/10.1029/2007PA001471.

Liu, Q., Torrent, J., Maher, B. A., Yu, Y., Deng, C., Zhu, R., & Zhao, X. (2005). Quantifying grain size distribution of pedogenic magnetic particles in Chinese loess and its significance for pedogenesis, *Journal of Geophysical Research*, *110*, B11102, https://doi.org/10.1029/2005JB003726.

Lovely, D. R., Stolz, J. F., Nord, G. L., & Phillips, E. J. P. (1987). Anaerobic production of magnetite by a dissimilatory iron-reducing microorganism. *Nature*, *330*, 252–254, https://doi.org/10.1038/330252a0.

Ludwig, P., Egli, R., Bishop, S., Chernenko, V., Frederichs, T., Rugel, G., et al. (2013). Characterization of primary and secondary magnetite in marine sediment by combining chemical and magnetic unmixing techniques. *Global and Planetary Change*, *110*, 321–339, https://doi.org/10.1016/j.gloplacha.2013.08.018.

Mao, X., Egli, R., Petersen, N., Hanzlik, M., & Liu, X. (2014). Magneto-chemotaxis in sediment: first insights. *PLoS ONE*, *9*, e102810, https://doi.org/10.1371/journal.pone.0102810.

McCausland, H. C., & Komeili, A. (2020). Magnetic genes: Studying the genetics of biomineralization in magnetotactic bacteria. *PLoS Genetics*, *16*, e1008499. https://doi.org/10.1371/journal.pgen.1008499.

Thomas, J. M., Simpson, E. T., Kasama, T., & Dunin-Borkowski, R. E. (2008). Electron holography for the study of magnetic nanomaterials, *Accounts of Chemical Research*, *41*, 665–674, https://doi.org/10.1021/ar700225v.

Miot, J., Benzerara, K., Morin, G., Kappler, A., Bernard, S., Obst, M., Férard, C., Skouri-Panet, F., Guigner, J.-M., Posth, N., Galvez, M., Brown, G. E., & Guyot, F. (2009). Iron biomineralization by anaerobic neutrophilic iron-oxidizing bacteria, *Geochimica et Cosmochimica Acta*, *73*, 696–711, https://doi.org/10.1016/j.gca.2008.10.033.

Miot, J., Li, J., Benzerara, K., Sougrati, M. T., Ona-Nguema, G., Bernard, S., Jumas, J.-C., & Guyot, F. (2014). Formation of single domain magnetite by green rust oxidation promoted by microbial anaerobic nitrate-dependent iron oxidation, *Geochimica et Cosmochimica Acta*, *139*, 327–343, https://doi.org/10.1016/j.gca.2014.04.047.

Monteil, C. L., Grouzdev, D. S., Perrière, G., Alonso, B., Rouy, Z., Cruveiller, S., et al. (2020). Repeated horizontal gene transfers triggered parallel evolution of magnetotaxis in two evolutionary divergent lineages of magnetotactic bacteria. *The ISME Journal*, *14*, 1783–1794, https://doi.org/10.1038/s41396-020-0647-x.

Moskowitz, B., Frankel, R., & Bazylinski, D. (1993). Rock Magnetic Criteria for the Detection of Biogenic Magnetite. *Earth and Planetary Science Letters*, *120*, 283–300, https://doi.org/10.1016/0012-821X(93)90245-5.

Moskowitz, B. M., Frankel, R. B., Walton, S. A., Dickson, D. P. E., Wong, K. K. W., Douglas, T., & Mann S. (1997). Determination of the preexponential frequency factor for superparamagnetic maghemite particles in magnetoferritin. *Journal of Geophysical Research*, *102*, 22,671–22,680, https://doi.org/10.1029/97JB01698.

Müller, F. D., Schüler, D., & Pfeiffer, D. (2020). A compass to boost navigation: Cell biology of bacterial magnetotaxis. *Journal of Bacteriology*, *202*, https://doi.org/10.1128/JB.00398-20.

Murat, D., Quinlan, A., Vali, H., & Komeili, A. (2010). Comprehensive genetic dissection of the magnetosome gene island reveals the step-wise assembly of a prokaryotic organelle. *Proceedings of the National Academy of Sciences of the United States of America*, *107*, 5593–5598, https://doi.org/10.1073/pnas.0914439107.

Muxworthy, A., & Williams, W. (2005). Magnetostatic interaction fields in first-order-reversal-curve diagrams. *Journal of Applied Physics*, *97*, 063905, https://doi.org/10.1063/1.1861518.

Muxworthy, A. R., & Williams, W. (2006). Critical single-domain/multidomain grain sizes in noninteracting and interacting elongated magnetite particles: Implications for magnetosomes. *Journal of Geophysical Research: Solid Earth*, *111*, B12S12, https://doi.org/10.1029/2006JB004588.

Muxworthy, A., Williams, W., & Virdee, D. (2003). Effect of magnetostatic interactions on the hysteresis parameters of single-domain and pseudo-single-domain grains. *Journal of Geophysical Research: Solid Earth*, *108*, 2517, https://doi.org/10.1029/2003JB002588.

Newell, A. J. (2005). A high-precision model of first-order reversal curve (FORC) functions for single-domain ferromagnets with uniaxial anisotropy. *Geochemistry Geophysics Geosystems*, *6*, Q05010, https://doi.org/10.1029/2004GC000877.

Newell, A. J. (2009). Transition to superparamagnetism in chains of magnetosome crystals. *Geochemistry Geophysics Geosystems*, *10*, Q11Z08, https://doi.org/10.1029/2009GC002538.

Oda, H., Nakasato, Y., & Usui, A. (2018). Characterization of marine ferromanganese crust from the Pacific using residues of selective chemical leaching: identification of fossil magnetotactic bacteria with FE-SEM and rock magnetic methods, *Earth, Planets and Space*, *70*, 165, https://doi.org/10.1186/s40623-018-0924-3.

Oldfield, F. (2007). Sources of fine-grained magnetic minerals in sediments: a problem revisited. *The Holocene*, *17*, 1265–1271, https://doi.org/10.1177/0959683607085135.

1483 Ouyang, T., Heslop, D., Roberts, A. P., Tian, C., Zhu, Z., Qiu, Y., & Peng, X. (2014).
1484 Variable remanence acquisition efficiency in sediments containing biogenic and
1485 detrital magnetites: Implications for relative paleointensity signal recording.
1486 *Geochemistry Geophysics, Geosystems*, *15*, 2780–2796,
1487 https://doi.org/10.1002/2014GC005301.

1488 Pan, Y. X., Petersen, N., Winklhofer, M., Davila, A. F., Liu, Q. S., Frederichs, T., et al.
1489 (2005). Rock magnetic properties of uncultured magnetotactic bacteria. *Earth and*
1490 *Planetary Science Letters*, *237*, 311–325, https://doi.org/10.1016/j.epsl.2005.06.029.

1491 Petermann, H., & Bleil, U. (1993). Detection of live magnetotactic bacteria in South
1492 Atlantic deep-sea sediments, *Earth and Planetary Science Letters*, *117*, 223–228,
1493 https://doi.org/10.1016/0012-821X(93)90128-V.

1494 Petersen, N., von Dobeneck, T., & Vali, H. (1986). Fossil bacterial magnetite in deep-sea
1495 sediments from the South Atlantic Ocean. *Nature*, *320*, 611–615. https://doi.org/
1496 10.1038/320611a0.

1497 Philipse, A. P., & Maas, D. (2002). Magnetic colloids from magnetotactic bacteria: Chain
1498 formation and colloidal stability. *Langmuir*, *18*, 9977–9984. https://doi.org/10.1021/
1499 la0205811.

1500 Pike, C. R., Roberts, A. P., & Verosub, K. L. (2001). First-order reversal curve diagrams
1501 and thermal relaxation effects in magnetic particles, *Geophysical Journal*
1502 *International*, *145*, 721–730, https://doi.org/10.1046/j.0956-540x.2001.01419.x.

1503 Rioux, J.-B., Philippe, N., Pereira, S., Pignol, D., Wu, L.-F., & Ginet, N. (2010). A
1504 Second Actin-Like MamK Protein in Magnetospirillum magneticum AMB-1 Encoded
1505 Outside the Genomic Magnetosome Island. *PLoS ONE*, *5*, e9151,
1506 https://doi.org/10.1371/ journal.pone.0009151.

1507 Roberts, A. P., Almeida, T. P., Church, N. S., Harrison, R. J., Heslop, D., Li, Y., et al.
1508 (2017). Resolving the origin of pseudo-single domain magnetic behavior. Journal of
1509 *Geophysical Research: Solid Earth*, *122*, 9534–9558, https://doi.org/10.1002/
1510 2017JB014860.

1511 Roberts, A. P., Chang, L., Heslop, D., Florindo, F., & Larrasoaña, J. C. (2012). Searching
1512 for single domain magnetite in the "pseudo-single-domain" sedimentary haystack:
1513 Implications of biogenic magnetite preservation for sediment magnetism and relative
1514 paleointensity determinations. *Journal of Geophysical Research: Solid Earth*, *117*,
1515 B08104, https://doi.org/10.1029/2012JB009412.

1516 Roberts, A. P., Florindo, F., Villa, G., Chang, L., Jovane, L., & Bohaty, S. M., et al.
1517 (2011). Magnetotactic bacterial abundance in pelagic marine environments is limited
1518 by organic carbon flux and availability of dissolved iron. *Earth and Planetary Science*
1519 *Letters*, *310*, 441–452, https://doi.org/10.1016/j.epsl.2011.08.011.

1520 Roberts, A. P., Hu, P., Harrison, R. J., Heslop, D., Muxworthy, A. R., Oda, H., Sato, T.,
1521 Tauxe, L., & Zhao, X. (2019). Domain state diagnosis in rock magnetism: Evaluation
1522 of potential alternatives to the Day diagram, *Journal of Geophysical Research: Solid*
1523 *Earth*, *124*, 5286–5314, https://doi.org/10.1029/2018JB017049.

1524 Ruder, W. C., Hsu, C.-P. D., Edelman, B. D., Schwartz, R., & LeDuc, P. R. (2012).
1525 Biological colloid engineering: Self-assembly of dipolar ferromagnetic chains in a
1526 functionalized biogenic ferrofluid. *Applied Physics Letters*, *101*, 063701, https://
1527 doi.org/10.1063/1.4742329.

1528 Scheffel, A., Gruska, M., Faivre, D., Linaroudis, A., Plitzko, J. M., & Schüler, D. (2006).
1529 An acidic protein aligns magnetosomes along a filamentous structure in magnetotactic
1530 bacteria. *Nature*, *440*, 110–114, https://doi.org/10.1038/nature04382.

1531 Schüler, D., Uhl, R., & Bäuerlein, E. (1995). A simple light scattering method to assay
1532 magnetism in Magnetospirillum gryphiswaldense, *FEMS Microbiology Letters*, *132*,
1533 139–145, https://doi.org/10.1016/0378-1097(95)00300-T.

1534 Shcherbakov, V. P., Winklhofer, M., Hanzlik, M., & Petersen, N. (1997). Elastic stability
1535 of chains of magnetosomes in magnetotactic bacteria. *European Biophysics Journal*,
1536 *4*, 319–326, https://doi.org/10.1007/s002490050086.

1537 Simmons, S. L., Sievert, S. M., Frankel, R. B., Bazylinski, D. A., & Edwards, K. J.
1538 (2004). Spatiotemporal distribution of marine magnetotactic bacteria in a seasonally
1539 stratified coastal salt pond. *Applied and Environmental Microbiology*, *70*, 6230–6239,
1540 https://doi.org/10.1128/AEM.70.10.6230-6239.2004.

1541 Simpson, E. T., Kasama, T., Pósfai, M., Buseck, P. R., Harrison, R. J., & Dunin-
1542 Borkowski, R. E. (2005). Magnetic induction mapping of magnetite chains in
1543 magnetotactic bacteria at room temperature and close to the Verwey transition using
1544 electron holography. *Journal of Physics: Conference Series*, *17*, 108–121,
1545 https://doi.org/ 10.1088/1742-6596/17/1/017.

Snoeck, E., Houdellier, F., Taniguch, Y., Masseboeuf, A., Gatel, C., Nicolai, J., & Hytch, M. (2014). Off-Axial Aberration Correction using a B-COR for Lorentz and HREM Modes. *Microscopy and Microanalysis*, *20*, 932–933, https://doi.org/10.1017/S1431927614006382.

Takeno, Y., Murakami, Y., Sato, T., Tanigaki, T., Soon Park, H., Shindo, D., Ferguson, M. R., & Krishnan, K. M. (2014). Morphology and magnetic flux distribution in superparamagnetic single-crystalline Fe_3O_4 nanoparticle rings. *Applied Physics Letters*, *105*, 183102, https://doi.org/10.1063/1.4901008.

Tang, F., Taylor, R. M. J., Einsle, J. F., Borlina, C. S., Fu, R. R., Weiss, B. P., Williams, H. M., Williams, W., Nagy, L., Midgley, P. A., Lima, E. A., Bell, E. A., Harrison, T. M., Alexander, E. W., & Harrison, R. J. (2019). Secondary magnetite in ancient zircon precludes analysis of a Hadean geodynamo, *Proceedings of the National Academy of Sciences of the United States*, *116*, 407–412, https://doi.org/10.1073/pnas.1811074116.

Taoka, A., Kondo, J., Oestreicher, Z., & Fukumori, Y. (2014). Characterization of uncultured giant rod-shaped magnetotactic Gammaproteobacteria from a freshwater pond in Kanazawa, Japan. *Microbiology*, *160*, 2226–2234, https://doi.org/10.1099/mic.0.078717-0.

Tauxe, L., Butler, R. F., Van der Voo, R., & Banerjee, S. K. (2010). *Essentials of Paleomagnetism*, University of California Press.

Thomas-Keprta, K. L., Bazylinski, D. A., Kirschvink, J. L., Clemett, S. J., McKay, D. S., Wentworth, S. J., Vali, H., Gibson, E. K., & Romanek, C. S. (2000). Elongated prismatic magnetite crystals in ALH84001 carbonate globules: Potential Martian magnetofossils. *Geochimica et Cosmochimica Acta*, *64*, 4049–4081, https://doi.org/10.1016/S0016-7037(00)00481-6.

Till, J. L., Guyodo, Y., Lagroix, F., Morin, G. Menguy, N., & Ona-Nguema, G. (2017). Presumed magnetic biosignatures observed in magnetite derived from abiotic reductive alteration of nanogoethite, *Comptes Rendus Geoscience*, *349*, 63–70, https://doi.org/ 10.1016/j.crte.2017.02.001.

Uebe, R., & Schueler, D. (2016). Magnetosome biogenesis in magnetotactic bacteria. *Nature Reviews Microbiology*, *14*, 621–637, https://doi.org/10.1038/nrmicro.2016.99.

1577 Ustra, A. T., Mendonça, da Silva Leite, A., Macouin, M., Doherty, R., Respaud, M., &
1578 Tocuti, G. (2021). Ultrafine magnetic particles: A DIET-proxy in organic rich
1579 sediments?, *Frontiers in Earth Sciences*, *8*, 754, https://doi.org/10.3389/feart.2020.
1580 608387.

1581 Usui, Y., Yamazaki, T., & Saitoh, M. (2017). Changing Abundance of Magnetofossil
1582 Morphologies in Pelagic Red Clay Around Minamitorishima, Western North Pacific.
1583 *Geochemistry Geophysics Geosystems*, *18*, 4558–4572, https://doi.org/10.1002/
1584 2017GC007127.

1585 Vali, H., Förster, O., Amarantidis, G., & Petersen, N. (1987). Magnetotactic bacteria and
1586 their magnetofossils in sediments, *Earth and Planetary Science Letters*, *86*, 389–400,
1587 https://doi.org/10.1016/0012-821X(87)90235-4.

1588 Varón, M., Beleggia, M., Kasama, T., Harrison, R. J., Dunin-Borkowski, R. E., Puntes,
1589 V. F., & Frandsen, C. (2013). Dipolar magnetism in ordered and disordered low-
1590 dimensional nanoparticle assemblies. *Scientific Reports*, *3*, 1234, https://doi.org/
1591 10.1038/srep01234.

1592 Volkov, V. V., Han, M. G., & Zhu, Y. (2013). Double-resolution electron holography
1593 with simple Fourier transform of fringe-shifted holograms. *Ultramicroscopy*, *134*,
1594 175–184, https://doi.org/10.1016/j.ultramic.2013.06.018.

1595 Wagner, C. L., Lascu, I., Lippert, P. C., Egli, R., Livi, K. J. T. & Sears, H. B. (2021).
1596 Diversification of iron-biomineralizing organisms during the Paleocene-Eocene
1597 Thermal Maximum: Evidence from quantitative unmixing of magnetic signatures of
1598 conventional and giant magnetofossils. *Paleoceanography and Paleoclimatology*, *36*,
1599 e2021PA004225, https://doi.org/10.1029/2021PA004225.

1600 Wang, H., Kent, D. V., & Jackson, M. J. (2013). Evidence for abundant isolated magnetic
1601 nanoparticles at the Paleocene-Eocene boundary, *Proceedings of the National*
1602 *Academy of Sciences of the United States*, *110*, 425–430, https://doi.org/10.1073/pnas.
1603 1205308110.

1604 Wang, Y., Lin, W., Li, J., Zhang, T., Li, Y., Tian, J., Gu, L., Van der Heyden, Y., & Pan,
1605 Y. (2015). Characterizing and optimizing magnetosome production of *Magneto-*
1606 *spirillum* sp. XM-1 isolated from Xi'an City Moat, China, *FEMS Microbiology*
1607 *Letters*, *362*, fnv167, https://doi.org/10.1093/femsle/fnv167.

Wang, X., Zheng, H., Wang, Q., Jiang, W., Wen, Y., Tian, J., Sun, J., Li, Y., & Li, J. (2019). Novel protein Mg2046 regulates magnetosome synthesis in Magnetospirillum gryphiswaldense MSR-1 by modulating a proper redox status, *Frontiers in Microbiology*, *10*, 1478, https://doi.org/10.3389/fmicb.2019.01478.

Weiss, B. P., Kim, S. S., Kirschvink, J. L., Kopp, R. E., Sankaran, M., Kobayashi, A. & Komeili, A. (2004). Magnetic tests for magnetosome chains in Martian meteorite ALH84001. *Proceedings of the National Academy of Sciences of the United States*, *101*, 8281–8284, https://doi.org/10.1073/pnas.0402292101.

Yamazaki, T., Fu, W., Shimono, T., & Usui, Y. (2020). Unmixing biogenic and terrigenous magnetic mineral components in red clay of the Pacific Ocean using principal component analyses of first-order reversal curve diagrams and paleoenvironmental implications. *Earth Planets Space*, *72*, 120, https://doi.org/10.1186/s40623-020-01248-5.

Yamazaki, T., & Kawahata, H. (1998). Organic carbon flux controls the morphology of magnetofossils in marine sediments, *Geology*, *26*, 1064–1066, https://doi.org/10.1130/0091-7613(1998)026<1064:OCFCTM>2.3.CO;2.

Zhang, H., Menguy, N., Wang, F., Benzerara, K., Leroy, E., Liu, P., et al. (2017). Magnetotactic Coccus Strain SHHC-1 Affiliated to Alphaproteobacteria Forms Octahedral Magnetite Magnetosomes. *Frontiers in Microbiology*, *8*, 969, https://doi.org/10.3389/fmicb.2017.00969.

Zhao, X., Egli, R., Gilder, S. A., & Müller, S. (2016). Microbially assisted recording of the Earth's magnetic field in sediment, *Nature Communications*, *7*, 10673, https://doi.org/ 10.1038/ncomms10673.

Zhao, X., Fujii, M., Suganuma, Y. Zhao, X., Jiang, Z. (2018). Applying the Burr Type XII distribution to decompose remanent magnetization curves. *Journal of Geophysical Research*, *123*, 8298–8311, https://doi.org/10.1029/2018JB016082.

Tables

Table 1. Summary of measured and modelled magnetic properties of MTB, magneto-fossils, and other SD particle assemblages. M_{rs}/M_s is the ratio between the central ridge magnetization and the saturation remanent magnetization, χ_a/M_{rs} is the so-called ARM ratio, and M_{cr}/M_s the ratio between the total magnetization of the central ridge and the saturation magnetization.

Structure	Reference	M_{rs}/M_s	χ_a/M_{rs} (mm/A)	M_{cr}/M_{rs}
Natural sediment				
Lake Baldeggersee	Egli (2004), Wagner et al., (2021)	0.41	2–4	0.37
Lake Ely	Egli et al. (2010)	0.47	—	0.48
Pelagic carbonate (CBD) [1]	Ludwig et al. (2013)	0.47	2–3	0.65
Paleosol S1 (CBD) [1]	Egli (2004, 2021)	0.20	1.7	0.32
Single-stranded chains				
Cultured MTB	Li et al. (2012), Moskowitz et al. (1993)	0.50	3.1–3.7	0.65
AMB-1	This study, Li et al. (2012)	0.48–0.50	1.38	0.79
Simulated	This study	0.49–0.50	—	0.71-0.72
Simulated	Chang et al. (2019)	0.32–0.50	—	—
Multistranded chains				
Wild-type MTB	Pan et al. (2005)	0.47–0.51	0.5–0.8	—
Simulated (2 strands)	This study	0.47–0.49	—	0.40–0.42
Simulated (fold-collapsed)	This study	0.47–0.50	—	0.37–0.38
Clumps and loops				
AMB-1 extract	Li et al. (2012)	0.22	0.23	—
MV-1 extract	Wang et al. (2013)	0.31	—	0.092
Δ*mamJ* mutant	Katzmann et al. (2013)	0.23	—	0.36
Δ*mamJ* Δ*limJ* mutant	This study	0.31	—	0.53
Extracellular magnetite				
Geobacter metallireducens	Moskowitz et al. (1993)	0.03	0.25	—
Shewanella putrefaciens	Carvallo et al. (2008)	0.14	—	—
Acidovorax on green rust	Miot et al. (2014)	—	—	0

[1] Citrate-Bicarbonate-Dithionite (CBD) extractable component calculated from the difference between pre- and post-CBD measurements.

Table 2. Boltzmann factors β_0 associated with the denucleation of high-moment states (HMS) and low-moment states (LMS) for various chain geometries with of N equidimensional magnetosomes of 50 nm diameter, separated by a diameter-normalized gap g.

Chain geometry	Gap g	N	β_0 (HMS)	β_0 (LMS)
Single-stranded	0.1	2	439.9	—
	0.1	7	763.9	—
	0.1	8	784.2	—
	0.1	9	795.0	—
	0.1	15	835.9	—
	0.1	16	839.7	—
	0.1	17	842.9	—
	0.05	17	969.2	—
Double-stranded (native)	0.1	10+9	667.8	800.4
	0.1	10+10	688.5	803.1
	0.1	11+10	705.2	801.6
	0.1	11+11	751.5	829.2
	0.05	11+11	864.0	953.4
Double-stranded (fold-collapsed)	0.1	10+9	235.0	1119
	0.1	10+10	268.4	1345
	0.1	11+10	277.7	1210
	0.1	11+11	242.2	1367
	0.05	11+11	278.5	1572
Ring	0.1	12	65.2	1518
	0.1	16	55.5	1606
	0.1	20	27.0	1633
	0.05	20	31.0	1877

1645 **Table 3.** Central ridge magnetization M_{cr} and total FORC magnetization M_{forc} from
1646 micromagnetic simulations of (1) single- and double-stranded chains, (2) a composite of
1647 intact chain configurations with a 2:1 proportion of equant vs. prismatic magnetosomes,
1648 (3) a composite of all chain configurations with 2:1 proportion of equant vs. prismatic
1649 magnetosomes (Figure 8b), and (4) the CBD-extractable fraction of a magnetofossil-rich
1650 pelagic carbonate from the Equatorial Pacific (Ludwig et al., 2013).

SD system	M_{cr}/M_s	M_{forc}/M_s	M_{cr}/M_{rs}	M_{cr}/M_{forc}
Stoner-Wohlfarth	0.272	0.272	0.544	1.0
Single-stranded equidimensional	0.347	0.379	0.704	0.914
Single-stranded prismatic	0.355	0.374	0.711	0.947
Double-stranded equidimensional	0.194	0.396	0.407	0.489
Double-stranded prismatic	0.209	0.367	0.424	0.570
Fold-collapsed equidimensional	0.171	0.397	0.366	0.431
Fold-collapsed prismatic	0.187	0.354	0.381	0.528
Composite chains (intact)	0.274	0.382	0.561	0.718
Composite chains (all)	0.242	0.382	0.500	0.632
Pelagic carbonate (CBD-extractable)	—	—	0.653	0.666

1651 **Table 4.** RPI parameters for different types of SD remanence carriers made of n SD
1652 crystals with mean magnetic moment m_{SD}. Other symbols: m_0 — native magnetic
1653 moment, m_{IRM} — magnetic moment after IRM acquisition, m_{ARM} — magnetic moment
1654 after ARM acquisition, r_a — ARM/IRM of isolated SD crystals.

SD configuration	**NRM** m_0/m_{SD}	**IRM** m_{IRM}/m_{SD}	**ARM** $m_{ARM}/r_a m_{SD}$	***R* (IRM)** m_0^2/m_{IRM}	***R* (ARM)** $r_a m_0^2/m_{ARM}$
Silicate inclusions	$\sim 0.9\sqrt{n}$	$\sim 0.5n$	$\sim 0.9\sqrt{n}$	~ 1.7	$\sim 0.9\sqrt{n}$
Single-stranded chains	n	$0.5n$	n	$2n$	n
Double-stranded chains	n	$0.5n$	δn	$2n$	$n^2/\delta n$
Fold-collapsed chains	δn	$0.5n$	δn	$2\delta n^2/n$	δn

Figure captions

Fig. 1. So-called Day diagram (Dunlop, 2002) showing the hysteresis properties $M_{\mathrm{rs}}/M_{\mathrm{s}}$ and $B_{\mathrm{cr}}/B_{\mathrm{c}}$ of intact cultured cells (Li et al., 2012; Moskowitz et al., 1993; Pan et al., 2005), SD particles in a magnetofossil-rich sediment (Ludwig et al., 2013), the AMB-1 mutant producing looped magnetosome arrangements (this work), and a Δ*mamJ* mutant producing magnetosome clusters (Katzmann et al., 2013). The properties of extracted magnetosomes (Li et al., 2012), micromagnetically simulated chains with increasing degree of axis randomization (Chang et al., 2019), and our micromagnetic simulations of intact and fold-collapsed chains are shown for comparison. Departures from $M_{\mathrm{rs}}/M_{\mathrm{s}} = 0.5$ for ideal, non-interacting, uniaxial SD particles (cultured cells), follow trends with increasing slopes, from intact and fold-collapsed configurations with strong uniaxial anisotropy to complete randomization (extracted magnetosomes), through the intermediate trend of looped and randomized chains.

Fig. 2. Representative examples of native and collapsed double-stranded magnetosome chains obtained from TEM micrographs. **(a)** Native, twisted double-stranded chain of equant magnetosomes produced by *M. gryphiswaldense*. Notice the magnetosome size tapering at both ends. **(b)** Native double-stranded chain of prismatic magnetosomes (Lefèvre et al., 2011). Notice the staggered magnetosome arrangement. **(c)** Top: kinked single-stranded chain of prismatic magnetosomes (Shcherbakov et al., 1997). Bottom: complete folding of a single-stranded chain around a kink point. Notice the side-by-side arrangement of magnetosomes, and one-sided tapering of magnetosome size. **(d)** Two examples of rings obtained from magnetophoresis of magnetosome chains extracted from cultures of *M. magnetotacticum* (Philipse and Maas, 2002).

Fig. 3. Electron microscopy images of wild-type and mutant AMB-1 cells.

Fig. 4. Numerically simulated zero-field magnetic states in idealized chains of identical magnetosomes with no magnetic anisotropy and dipolar interactions. The magnetic moments of individual crystals are indicated by arrows with the color coding corresponding to the axial component. **(a)** High-moment (SD-like) state of a single-stranded chain with 15 magnetosomes. **(b)** Two-domain state of the same chain as in (a), during a thermally activated magnetization reversal. **(c)** High-moment state of a ring with 20 magnetosomes, consisting of two symmetric domains with opposed vorticity. **(d)** Low-moment (FC) state of the same ring as in (c). **(e)** High-moment (SD-like) state of a double-stranded chain with 11+10 magnetosomes and staggered arrangement. **(f)** Low-moment (FC) state of the same double-stranded chain as in (e). See Supporting Movies S1-S4 for the corresponding transitions between states.

Fig. 5. Simulated FORC diagrams of single-stranded (left), native double stranded (middle) and fold-collapsed (right) chains of equidimensional (top) and prismatic (bottom) magnetite magnetosomes. Each FORC diagram corresponds to ~10^5 randomly oriented chains with a realistic distribution of geometric parameters as explained in the text. Coercivity distributions obtained from the simulated FORC data (f_{dcd} — DC demagnetization of saturation remanence, f_{hys} — irreversible component of the ascending hysteresis branch, f_{cr} — central ridge) are shown below, together with coercivity distributions of the biogenic component BS (gray lines in a-c) and BH (gray lines in d-f), obtained from AF demagnetization curves of ARM (from Egli, 2004a). All FORC diagrams share the same color scale (blue — negative values, green to violet — positive values) with q = 5, 10, 20, 30, 40, 50, 60, 70, 80, and 90% quantile contours. The FORC region enclosed by the q-quantile contour contributes to a fraction 1 – q of the total FORC integral (Egli, 2021). Dashed lines indicate the left boundary of the so-called memory region.

Fig. 6. Native magnetic states of wild-type AMB-1 and the AMB-1 mutant. Magnetization of a suspension of (a) wild-type and (d) mutant AMB-1 cells in small fields varying between ±2 mT, before (black) and after (gray) saturation in a 200 mT field. Electron microscopy and corresponding magnetic phase contours determined by off-axis electron holography images of (b-c) wild-type and (e-f) mutant magnetite chains.

Fig. 7. Magnetic properties of wild-type AMB-1 and the AMB-1 mutant. (a-b) FORC diagrams with 2, 5, 10, 20, 30, 40, 50, 60, 70, 80, 90% quantile contours. Insets are schematic representations of the magnetization of an individual cell as a function of the applied field. Numbers highlight the following features: 1 – central ridge created by the magnetization jump through which the lowest curve merges with curve I; 2 – positive and negative contributions from reversible magnetic moment rotation (difference between the slopes of consecutive curves); 3 — signatures of magnetically viscous particles (vertical ridge and central ridge extending to the origin); 4 — nucleation of a FC state from a negative SD state (contribution of the first magnetization jump in curve III to the difference between curves II and III); 5 — annihilation of a FC state (contribution of the magnetization jump in curve II to the difference between curves I and II); 6 — same as 5, but for the difference between curve II and III; 7 — annihilation of a FC state (contribution of the second magnetization jump in curve III to the difference between curves II and III). (c-d) Coercivity distributions of wild-type AMB-1 and the AMB-1 mutant, obtained from subsets of FORC data: f_{hys} — irreversible component of the ascending hysteresis branch, f_{dcd} — DC demagnetization of M_{rs}, f_{cr} — central ridge. The shaded area represents the f_{hys} contribution of SD magnetic states that cannot exist in a null field.

Fig. 8. Comparison between the FORC signature of SD particles in a magnetofossil-rich sediment and a simulated magnetofossil composite. **(a)** FORC diagram of in-situ <1μm magnetite particles (mostly SD) in a pelagic sediment (data from Ludwig et al., 2013). **(b)** FORC diagram of a simulated composite obtained from the six micromagnetically model-led chain structures, with the following relative contributions to the saturation magnetization, chosen for a visual match with the FORC diagram in (a): 1/3 single-stranded chains of equant magnetosomes, 1/6 single-stranded chains of prismatic magnetosomes, 1/3 native double-stranded chains of equant magnetosomes, 1/6 native double-stranded chains of prismatic magnetosomes, 1/3 fold-collapsed chains of equant magnetosomes, 1/6 fold-collapsed chains of prismatic magnetosomes. The same field range and contour levels with respect to the maximum amplitude are used in both plots to ease the comparison. Numbers highlight the following features: 1 — nucleation/annihilation of FC states, 2 — high-field limit of FC state nucleation/annihilation (asymmetric about the central ridge), 3 — residual negative amplitude from the annihilation of positive FC states, uncompensated by positive amplitudes from intermediate coercivity contributions.

Figure 1.

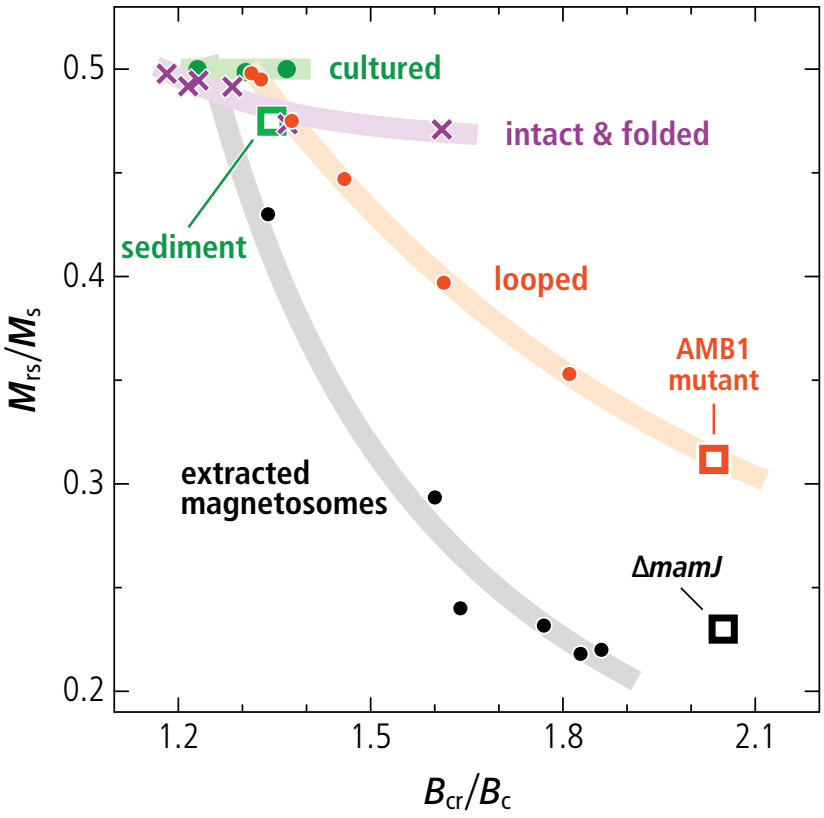
0.5
0.4
0.3
0.2
1.2
1.5
1.8
2.1
M_{rs}/M_s
B_{cr}/B_c
cultured
intact & folded
sediment
looped
AMB1
mutant
extracted
magnetosomes
ΔmamJ

Figure 2.

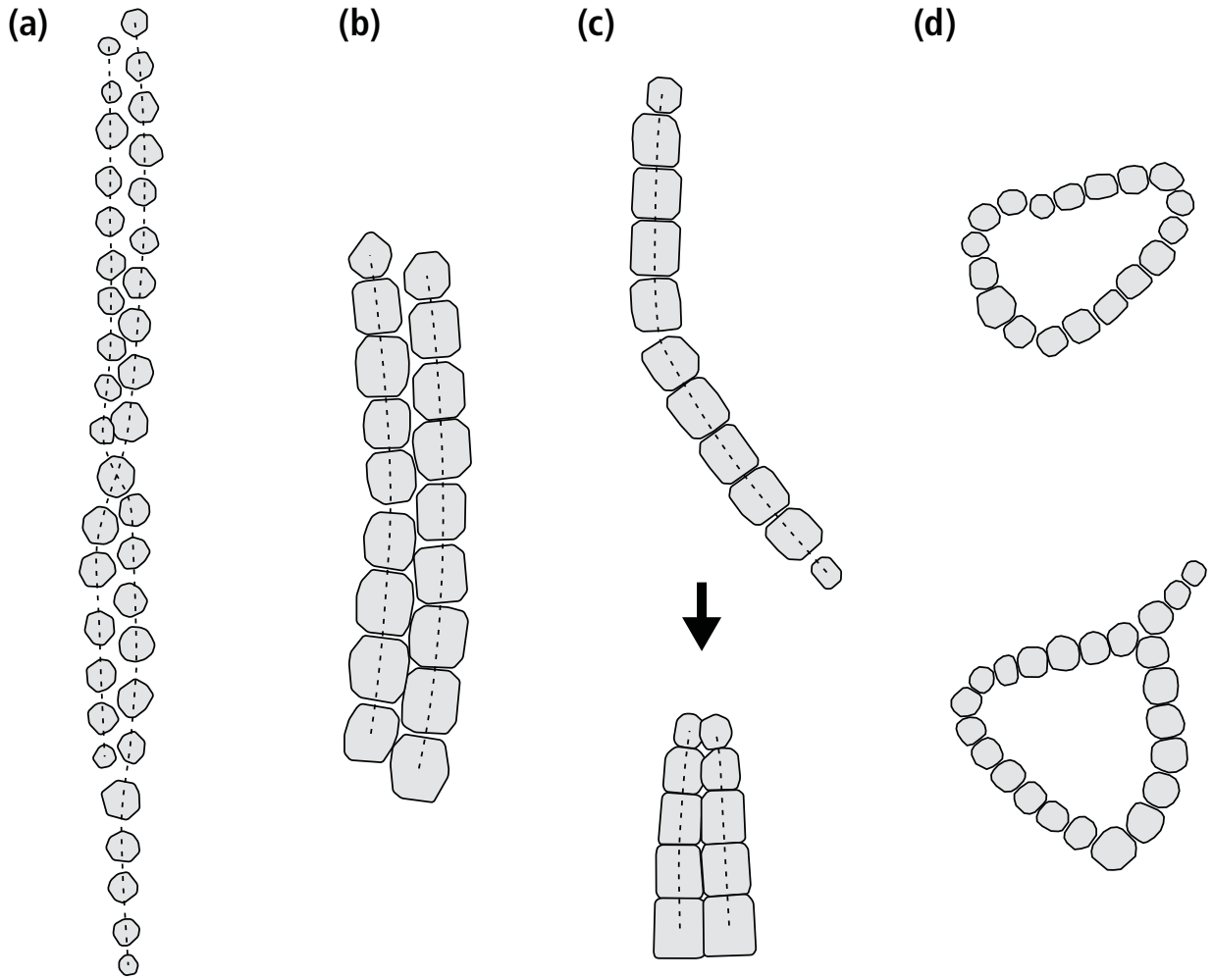
(a)
(b)
(c)
(d)

Figure 3.

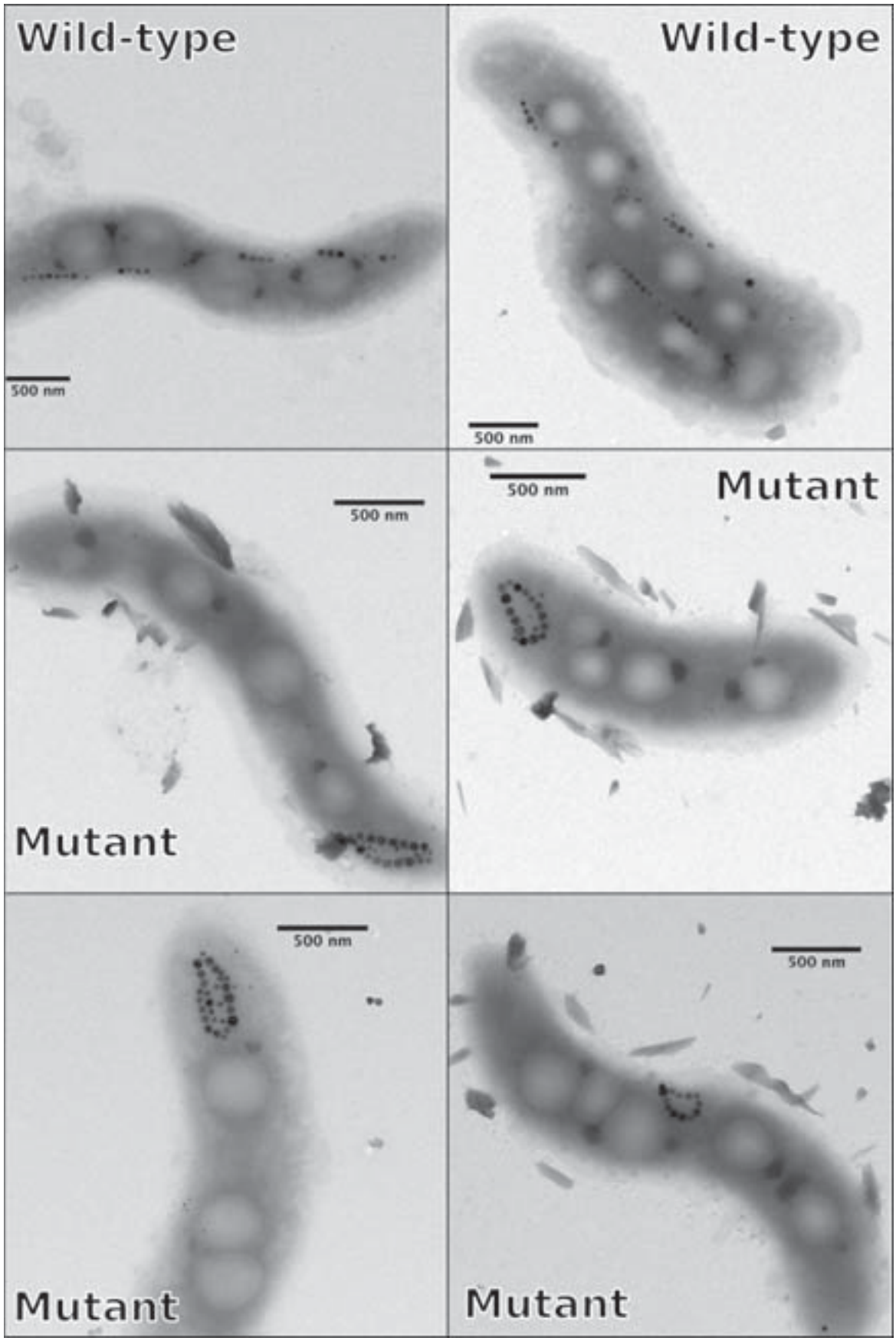
Wild-type
500 nm
Wild-type
500 nm
500 nm
Mutant
Mutant
500 nm
500 nm
Mutant

Figure 4.

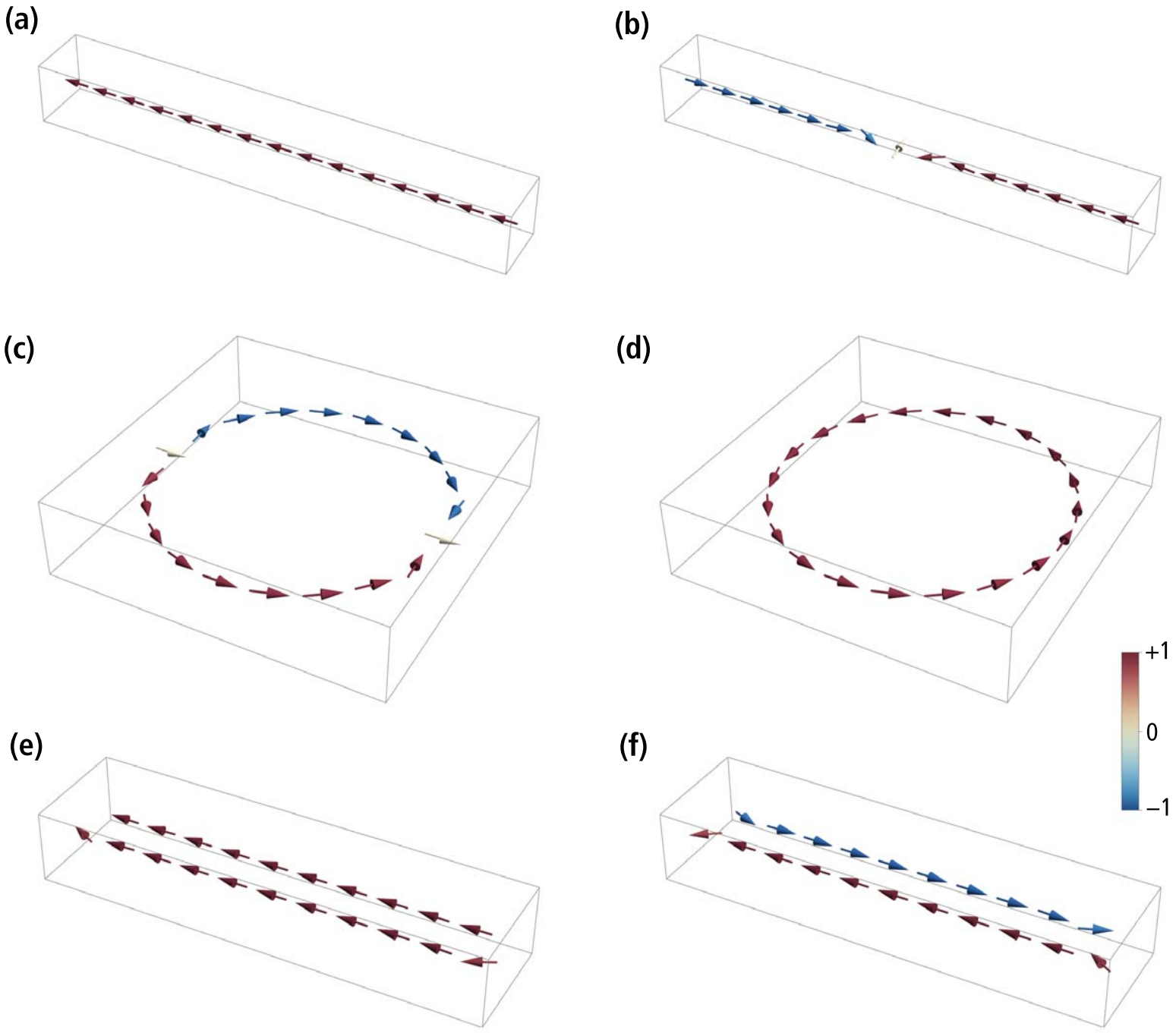
(a)
(b)
(c)
(d)
(e)
(f)
+1
0
−1

Figure 5.

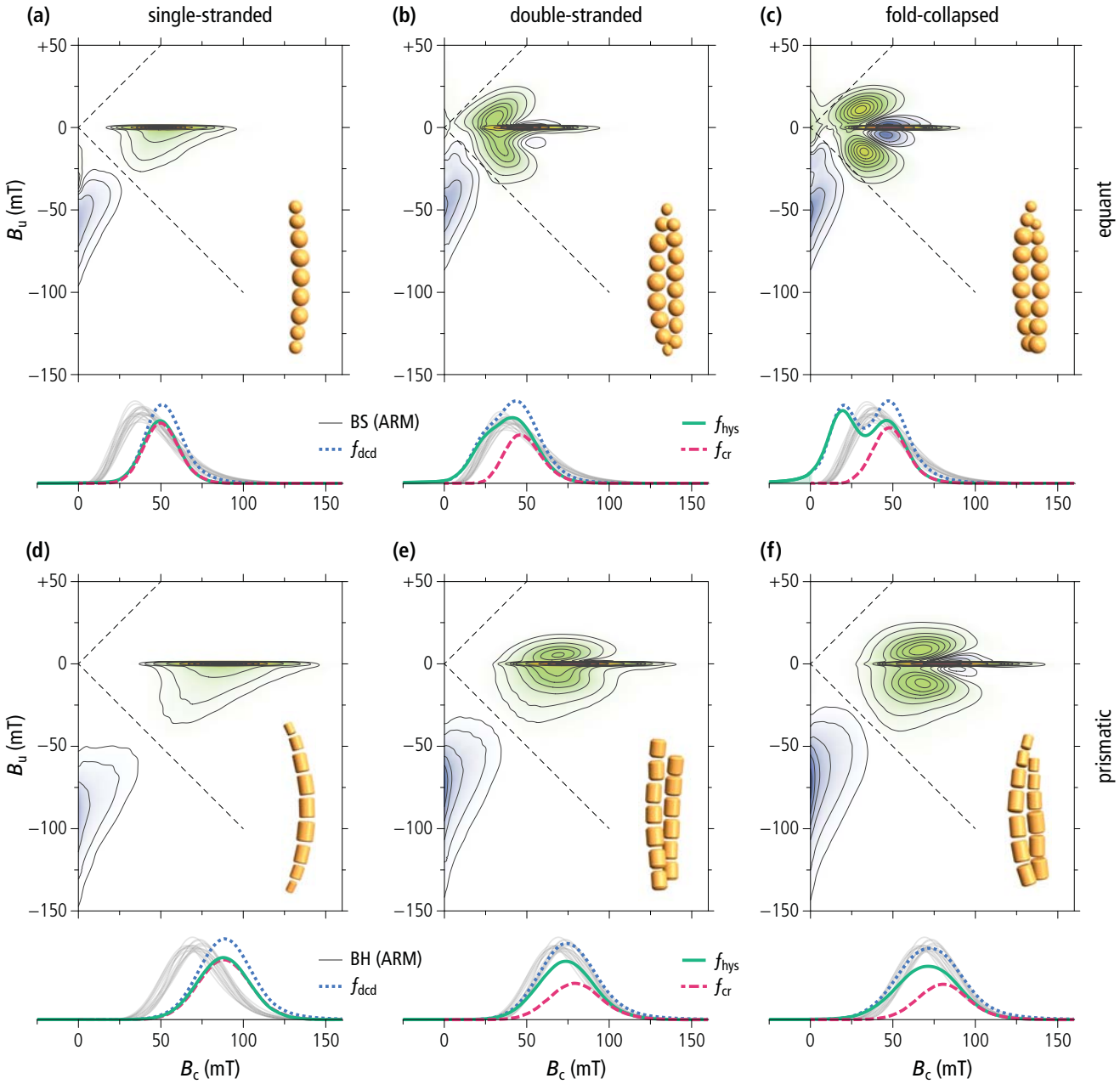
(a)
single-stranded
(b)
double-stranded
(c)
fold-collapsed
equant
(d)
(e)
(f)
prismatic
+50
0
−50
−100
−150
B_u (mT)
BS (ARM)
f_{dcd}
f_{hys}
f_{cr}
BH (ARM)
0
50
100
150
B_c (mT)

Figure 6.

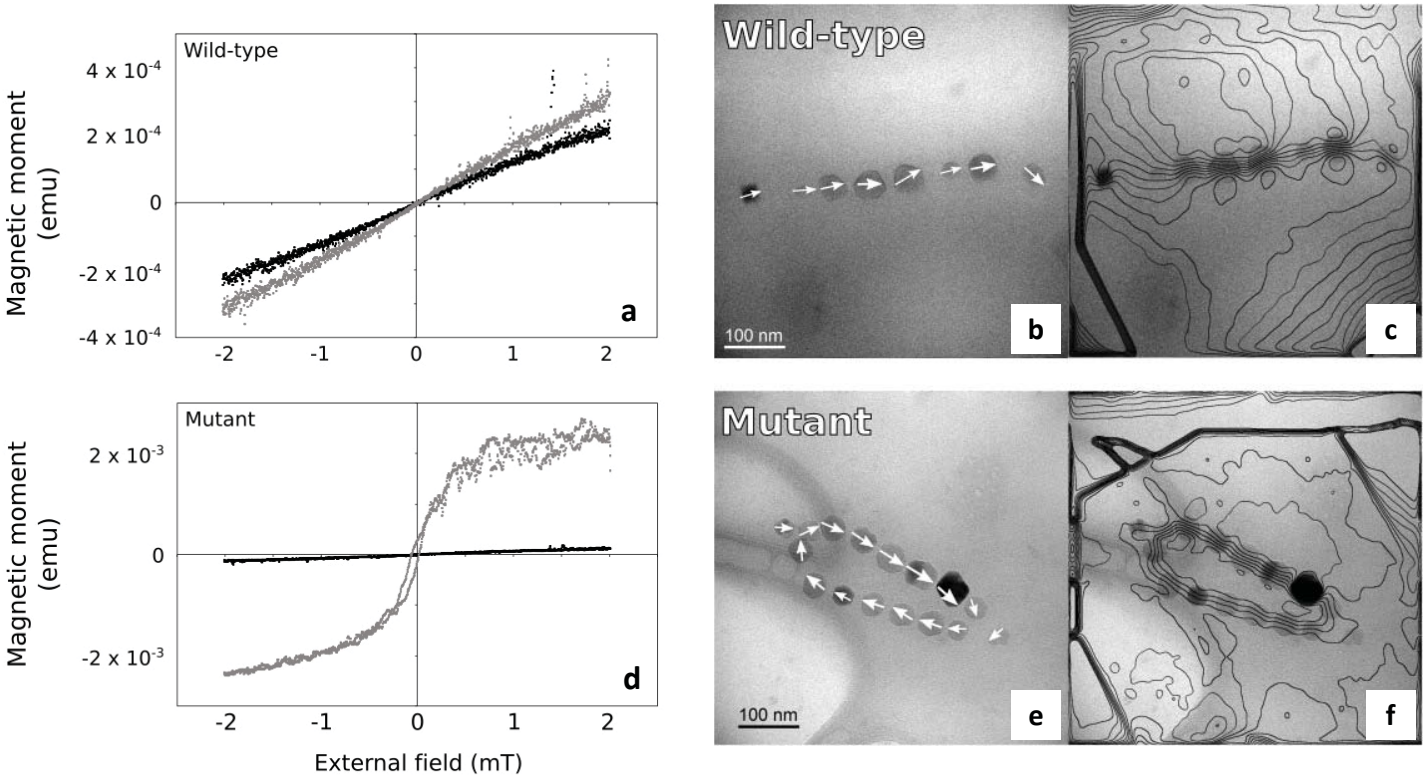
Wild-type
4 x 10-4
2 x 10-4
0
-2 x 10-4
-4 x 10-4
Magnetic moment (emu)
-2
-1
0
1
2
a
Mutant
2 x 10-3
0
-2 x 10-3
Magnetic moment (emu)
d
External field (mT)
Wild-type
100 nm
b
c
Mutant
100 nm
e
f

Figure 7.

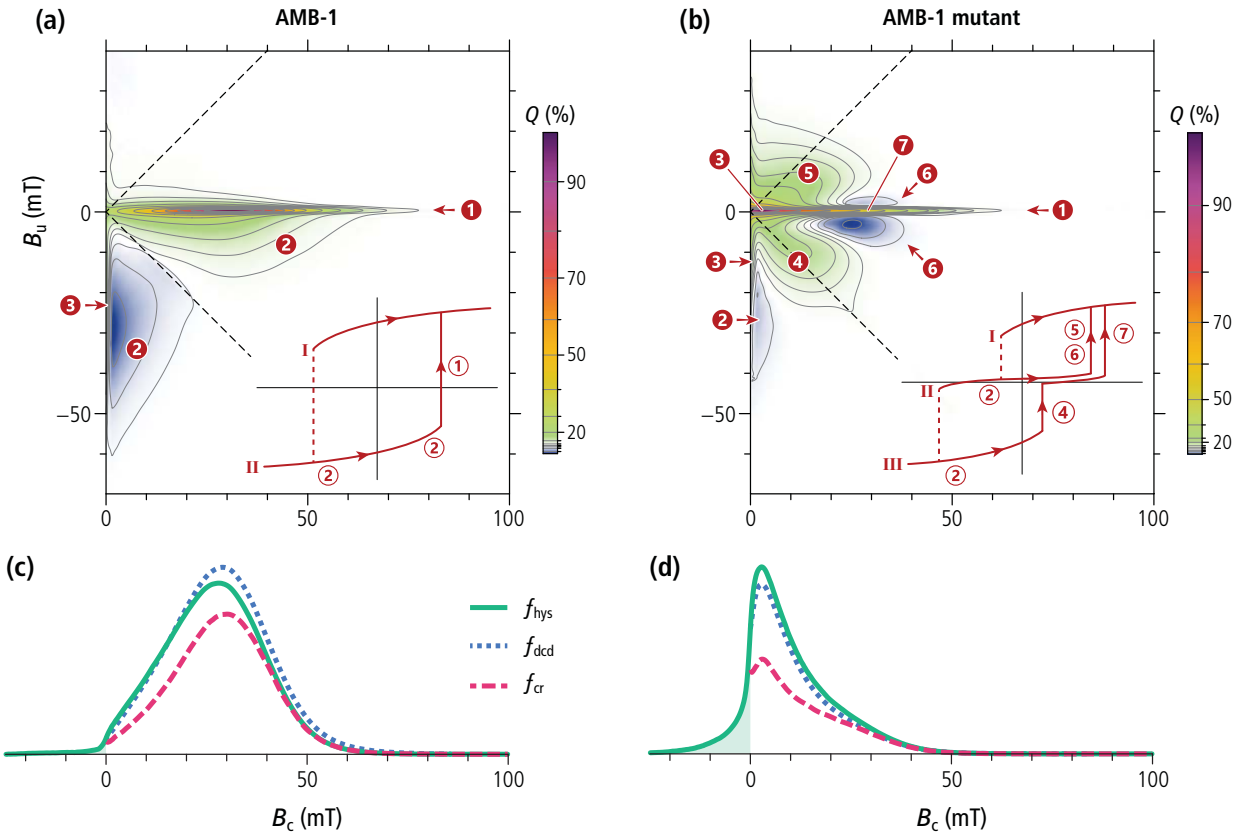
(a)
AMB-1
(b)
AMB-1 mutant
B_u (mT)
Q (%)
0
−50
50
100
90
70
50
20
I
II
III
(c)
(d)
f_{hys}
f_{dcd}
f_{cr}
B_c (mT)

Figure 8.

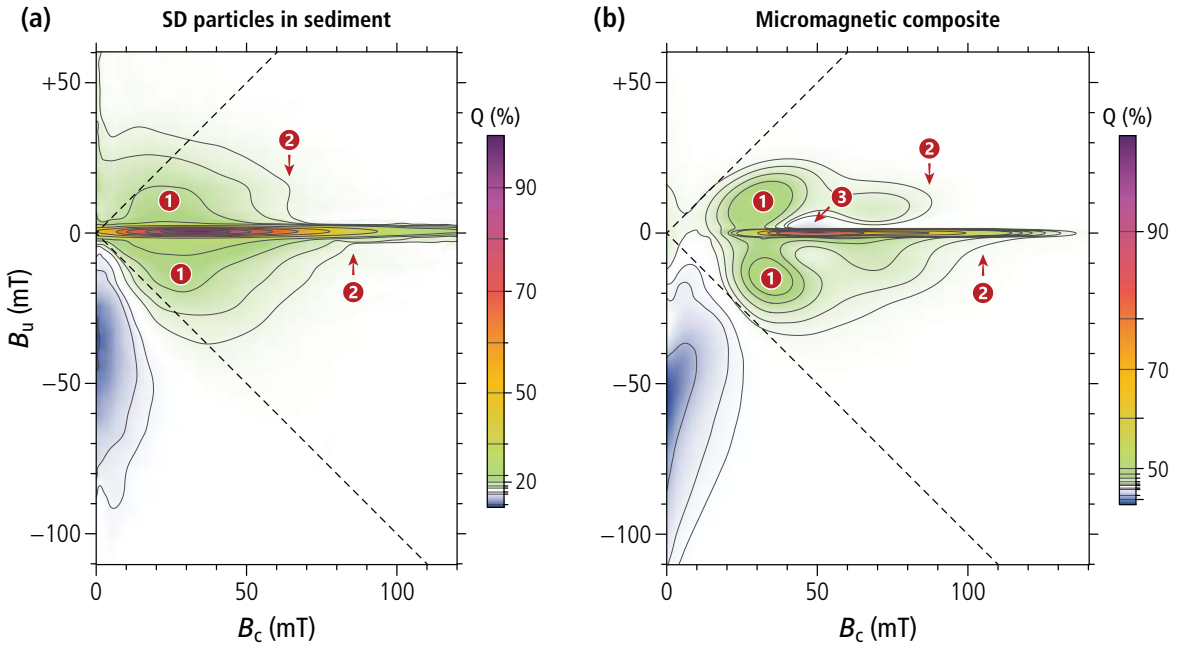
(a)
SD particles in sediment
(b)
Micromagnetic composite
Q (%)
90
70
50
20
+50
0
−50
−100
0
50
100
B_u (mT)
B_c (mT)
1
2
3